


COMPUTATION OF SNOWMELT AT A HIGH ARCTIC SITE



By   
Richard Heron, B.Sc.

A Thesis  
Submitted to the Faculty of Graduate Studies  
in Partial Fulfilment of the Requirements  
for the Degree  
Master of Science

McMaster University

February, 1979

COMPUTATION OF SNOWMELT AT A HIGH ARCTIC SITE

MASTER OF SCIENCE (1978)

(Geography)

McMASTER UNIVERSITY

Hamilton, Ontario

TITLE: Computation of Snowmelt at a High Arctic Site

AUTHOR: John Richard Heron, B.Sc. (Trent University)

SUPERVISOR: Professor M.K. Woo

NUMBER OF PAGES: ix, 89

## ABSTRACT

In 1977, snowmelt was studied at a site near Resolute Bay, N.W.T., with additional data obtained in 1978. Using measured net radiation and computed fluxes of sensible and latent heat, the surface energy balance over snow was calculated. Field measurements of snow ablation compared favourably with the computed values, indicating that the energy balance approach is adequate for the computation of snowmelt at a High Arctic site.

The surface energy balance was also extended to a number of slopes using data from the horizontal site. On individual clear or partly cloudy days, the difference in the surface energy balance between slopes was small and on overcast days, such differences were further minimized. Over the entire study period, computations show that there was little difference in the amount of energy received by various slopes up to  $10^{\circ}$ .

## ACKNOWLEDGMENTS

I wish to express my gratitude to my supervisor, Dr. M.M. Woo, for his guidance and encouragement in all phases of this study. I also wish to thank Dr. J.A. Davies for his advice and the loan of equipment, Dr. F.G. Hannell, Dr. W.P. Adams and Trent University, for the loan of equipment, and Philip Marsh and Jacques Sauriol for their companionship and assistance in the field.

This study was supported by grants from the National Research Council of Canada; Water Resources Research Support Program, Inland Waters Directorate, Department of Fisheries and the Environment; and the McMaster University Presidential Committee for Northern Studies. Generous logistical support was received from Polar Continental Shelf Project, Department of Energy, Mines and Resources.

Thanks also to the Polar Shelf staff at Resolute Bay: Fred, Bill, Emile, George and Lief, for their generous assistance, and to my mother, Vonnie Heron, for typing the final draft.

## TABLE OF CONTENTS

		PAGE
	ABSTRACT	iii
	ACKNOWLEDGMENTS	iv
	TABLE OF CONTENTS	v
	LIST OF FIGURES	vii
	LIST OF TABLES	viii
CHAPTER		
1	INTRODUCTION	1
	1.1 Literature Review	1
	1.2 Objective	2
2	SITE LOCATION AND INSTRUMENTATION	4
	2.1 Study Site	4
	2.1.1 Location and Topography	4
	2.1.2 Climate	4
	2.1.3 Snow Conditions	6
	2.2 Instrumentation and Methods	6
	2.2.1 Radiation	7
	2.2.2 Air Temperature and Humidity	8
	2.2.3 Wind	10
	2.2.4 Other Meteorological Variables	10
	2.2.5 Snow Measurements	12
	2.2.5.1 Snow Ablation	12
	2.2.5.2 Snow Density and Thermal Quality	13
	2.2.5.3 Snowpack Temperatures	14
3	SNOWMELT AT A SITE	15
	3.1 Snowcover Conditions	15
	3.2 Surface Energy Balance Equation	18
	3.3 Computed Surface Energy Balance	21
	3.4 Comparison of Calculated and Measured Values	27
	3.5 Development of the Boundary Layer	31
	3.6 Comparison with Results from Other Studies	34

CHAPTER		PAGE
4	SNOWMELT ON SLOPES	40
	4.1 Introduction	40
	4.2 Calculation of the Radiation Balance of Slopes	40
	4.2.1 Net Radiation on Slopes	40
	4.2.2 Direct Short-wave Radiation	42
	4.2.3 Diffuse Short-wave Radiation	46
	4.2.4 Reflected Short-wave Radiation	46
	4.2.5 Long-wave Radiation	48
	4.3 Results	50
	4.3.1 Albedo	50
	4.3.2 Slope Radiation Balance on Clear Days	58
	4.3.3 Slope Radiation Balance on Overcast Days	63
	4.3.4 Computation of Snowmelt on Slopes	63
5	CONCLUSION	71
	REFERENCES	73
	APPENDIX 1 Hourly Components of the Snow Surface Energy Balance	77
	APPENDIX 2 Notation	86

## LIST OF FIGURES

FIGURE		PAGE
2.1	Location of the experimental site, 3 km northeast of Resolute. Contours are at 5 m intervals above an arbitrary datum.	5
2.2	Construction of the radiation shield used for the temperature sensors in 1978.	9
2.3	Relationship between the 1 m wind speed at the study site and the 10 m wind speed at Resolute Airport weather station.	11
3.1	Thermal regime of the snowcover before and during the study period.	16
3.2	Development of ice lenses in typical snowcover profiles.	16
3.3	Spatial variation of the snowcover in the vicinity of the study site. The arrow points to meteorological site 1. The dates for these photos are June 8 (a), June 16 (b), June 20 (c), and June 29 (d).	17
3.4	Variation of air temperature, radiation and surface energy balance during the study period.	22
3.5	Diurnal variation of the surface energy balance components during an overcast day (above) and a clear day (below). $Q^*$ is the net radiation, $H$ is the sensible heat flux, $LE$ is the latent heat flux and $R$ is the energy from precipitation.	23
3.6	Daily variation of the energy balance components. The width of the arrow indicates the relative magnitude of the energy fluxes.	25
3.7	Comparison of cumulative calculated snowmelt and cumulative measured ablation.	28
3.8	Comparison of daily calculated snowmelt and daily observation ablation.	30
3.9	Temperature profiles above part of a snow patch showing development of a boundary layer as air is advected from left to right of the diagrams. The dots indicate the location of temperature measurement and the isotherms are in °C.	32



FIGURE		PAGE
3.10	Air temperature profiles over the snow surface on June 24, 1977.	33
4.1	Flow-chart for the computation of direct short-wave radiation received on a slope.	44
4.2	Decay of the snow surface albedo during the study period.	51
4.3	Relationship between solar elevation and snow albedo measured by the Atmospheric Environment Service at Resolute Bay.	52
4.4	Diurnal variation of albedo on north and south slopes during an overcast period.	53
4.5	Cloud cover and diurnal variation of albedo on a horizontal surface.	55
4.6	Relationship between albedo and solar elevation above the slope and horizontal, June 11, 1978.	56
4.7	Radiation balance on a horizontal surface on a clear day.	59
4.8	Radiation balance on slopes of 10° to 30° on a clear day. Values for the horizontal site have been included for comparative purposes.	60
4.9	Radiation balance on slopes during a cloudy day.	64
4.10	Cumulative snowmelt due to radiation in 10° slopes during the study period.	67
4.11	Cumulative snowmelt on 10° slopes during the study period.	69

## LIST OF TABLES

TABLE		PAGE
3.1	Daily totals of the surface energy balance components and daily ablation.	25
3.2	Summary of previous energy balance studies.	35
4.1	Total daily net radiation and snowmelt due to radiation on 12 slopes for a clear day, June 24, 1977.	61
4.2	Total daily net radiation and snowmelt due to radiation on 12 slopes for an overcast day, June 14, 1977.	65
4.3	Daily net radiation and cumulative snowmelt due to net radiation.	68

## CHAPTER ONE

### INTRODUCTION

#### 1.1 Literature Review

The importance of snowmelt in the runoff regime and water balance of High Arctic catchments has been emphasized in recent studies (Cogley 1975, Marsh 1978, McCann and Cogley 1972, Ryden 1977, Woo 1976). Most studies report that over 80 percent of the annual runoff occurs in two to three weeks during the snowmelt period. However, field studies on the snowmelt processes in the High Arctic remain scarce.

Studies of snowmelt processes have been carried out in a wide variety of non-Arctic locations, including glaciers (Föhn 1973, La Chapelle 1959, Lougeay 1974); snowfields (la Casinière 1974); alpine areas (U.S. Army 1956), as well as areas with thinner and sometimes patchy snowcovers (Granger and Male 1977, Gold and Williams 1960, McKay and Thurtell 1978). From such process studies, detailed models (Anderson 1976, Oblad and Rosse 1977) have been developed to compute the snowmelt occurring at these locations.

Snow and ice melt studies have also been conducted on Arctic glaciers and snowfields (Orvig 1954, Müller and Keeler 1969, Wendler and Ishikawa 1973) and results from these studies are comparable to those from more southerly latitudes except for the magnitude of ground heat

flux. However, the results of the Arctic tundra energy balance studies (Ohmura 1972, Ohmura and Müller 1976, Weller et al 1974) are different from those obtained on the prairies (Granger and Male 1977, O'Neill 1973), an environment somewhat comparable to the Arctic tundra.

The above mentioned studies are all site specific and do not incorporate variability due to slope angle and aspect. However, several procedures are available to determine the net radiation balance of a slope (Garnier and Ohmura 1968, Kondratyev 1969). Goodison 1972 compared snow ablation measurements to incident short-wave radiation estimated using the procedure outlined by Garnier and Ohmura (1968). In a much simplified approach, Price and Dunne (1976) used regression to estimate the net radiation on slopes which was then used to compute snowmelt. More complete slope radiation balance computations have been used in the snowmelt runoff models of Allen (1974) and O'Neill (1973).

Results from the studies mentioned above may not be directly applicable to the High Arctic in view of differences in environmental factors including snow distribution, snow properties and the duration of daylight hours during the melt period. There exists, therefore, a need to further our knowledge in the application of an energy balance technique to determine snowmelt in such an environment.

## 1.2 Objective

The objective of this study is to examine snowmelt processes in the High Arctic using an energy-balance approach. The surface energy balance will be first obtained for a horizontal site and then extended to

various slopes. Results from this study will contribute to a better understanding of snowmelt processes in the High Arctic as well as a more accurate prediction of snowmelt events.

## CHAPTER TWO

### SITE LOCATION AND INSTRUMENTATION

#### 2.1 Study Site

##### 2.1.1 Location and Topography

This study was carried out in a small catchment approximately 3 km northeast of Resolute Bay ( $74^{\circ} 43' N$ ,  $94^{\circ} 54' W$ ), Cornwallis Island, Northwest Territories (figure 2.1). The research site was located on gently undulating terrain. Nearby is a knoll approximately 50 m higher than the site. This knoll affects the fetch when a southerly wind blows. Wind fetch in other directions was limited by two small conical hills, the largest of which was sufficiently far away to the northwest (approximately 800 m) to produce significant effects. The other hill was 100 m to the north of the site and was much lower than the previous hill. At the centre of the study area was a small depression which was occupied by a stream and a small pond during the snowfree period. However, the site was flooded shortly after snowmelt started, and it was necessary to shift the sensors to higher grounds.

##### 2.1.2 Climate

Resolute Bay receives continuous daylight from the end of April to the middle of August. However, the solar elevations remain low, never reaching  $40^{\circ}$  above the horizon. Daily mean air temperature does not rise above freezing until June (Dept. of Transport, 1967). As a result, the melt period may occur from early June to mid-July. During the same period, the mean amount of cloud cover increases.



Fig. 2.1 Location of the experimental site, 3 km northeast of Resolute.  
 Contours are at 5 m intervals above an arbitrary datum.

Within the melt season, mean wind speed is the highest in June, reaching an average of 20.3 km/h (Dept. of Transport, 1967). The dominant wind direction is northwesterly with a frequency of 27 percent. South-easterly winds are also common at this time of year.

### 2.1.3 Snow Conditions

The entire study site is underlain by permafrost at an average depth of 0.5 m and the active layer remains frozen until the snow has melted. In 1977, the depth of snowcover at this site averaged 0.6 m. However, snow distribution was uneven. In early June, many ridges and hilltops were completely devoid of snow, while many of the smaller depressions and valleys were completely filled by snow. At the same time in the previous year, no bare ground was present in the study area. A difference in the snowcover conditions of the two years is due to the low winter precipitation of 1976-77, with 31 mm total snowfall water equivalent recorded by the Atmospheric Environment Service at Resolute Airport, compared with a long term mean of 72 mm (Dept. of Transport, 1974).

### 2.2 Instrumentation and Methods

During the study period, the instruments were shifted from one location to another. Such moves were necessitated by flooding, an increasing presence of bare ground or the unrepresentative nature of the snow surface. Thus some of the instrument locations shown in fig. 2.1 should be taken only as mean or representative locations.



### 2.2.1 Radiation

Net radiation was measured at a height of approximately 1.0 m above a horizontal snow surface using a Swisstecco SW-1 net radiometer. The readings were recorded on a Rustrak recorder. Measurements continued until late June when the diameter of the largest snowpatch was reduced to approximately 8 m. Under such conditions, the bare ground at the edge of the snow would also be sensed by the radiometer, and thus yielding an over estimate. To minimize this error, the measurement height was lowered to 0.75 m.

Additional radiation readings were taken by the Atmospheric Environment Service (A.E.S.) at the weather station at Resolute Airport. The radiation fields included incoming short-wave radiation ( $K_+$ ), and diffuse short-wave radiation ( $D$ ). Unfortunately, the snow at this location disappeared much earlier than at the study site. Thus, only the incoming short wave and diffuse short wave radiation components were used during the study period. Missing radiation data during this period were estimated by regression relationship obtained between various radiation components.

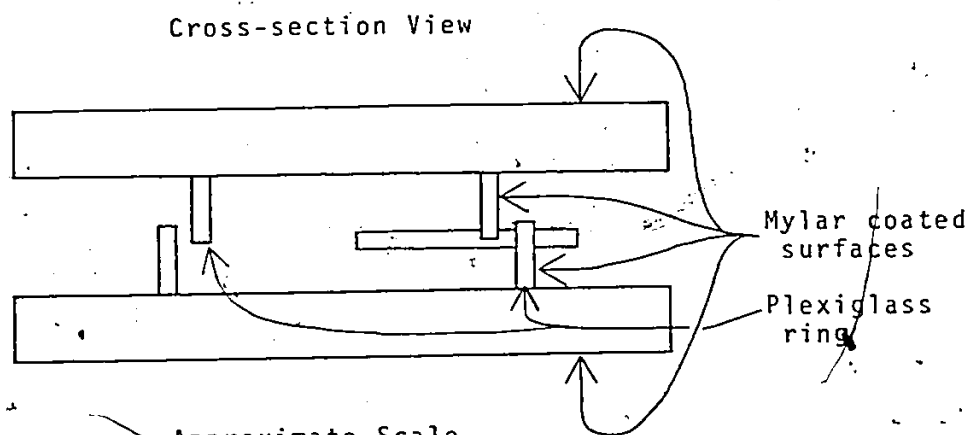
Snow surface albedo at the site was measured with a Monteith pyranometer whose signals were displayed on a Keithly digital multimeter. Manual readings were taken at irregular intervals next to the net radiometer and at the ablation study sites. However, instrument malfunctions resulted in a limited data base. Fortunately, the readings of  $K_+$  and  $K_+$  obtained at the weather station could be used to calculate the albedo of the snow, and this supplemented the albedo data.

### 2.2.2. Air Temperature and Humidity

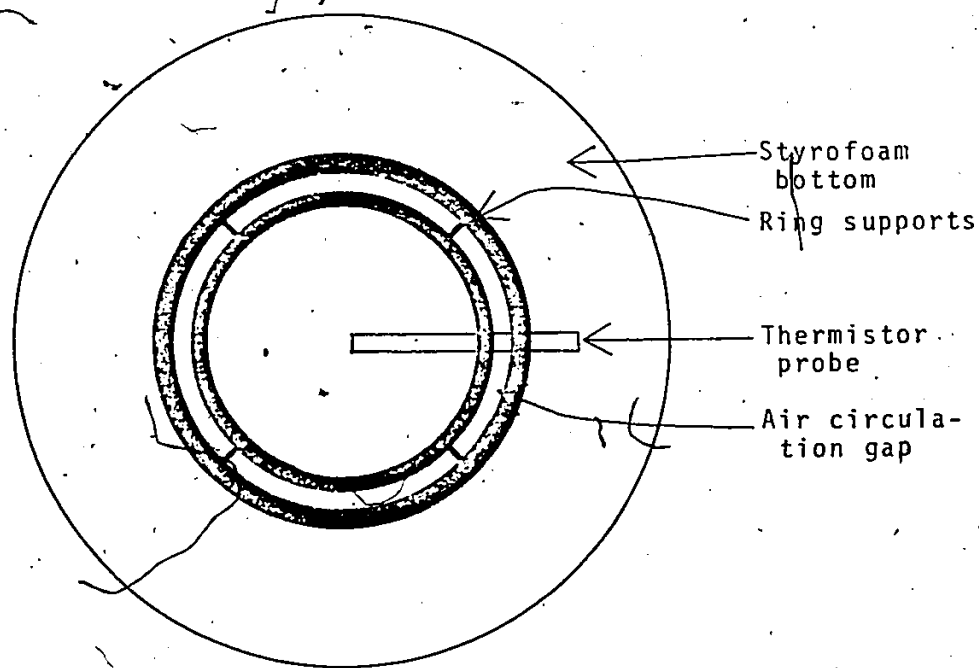
A continuous record of air temperature and humidity over snow was provided by a Lambrecht thermohygrograph housed in a Stevenson's screen 1 m above the snow surface. This instrument was calibrated with an Assman psychrometer. Missing data were estimated using a regression equation relationship between the Lambrecht and a Weather Measure thermohygrograph at meteorological site 1, both of which were read to 0.2°C.

In 1977, air temperature and humidity were measured at heights of 1.0 and 2.0 m above the snow surface, using shielded and ventilated psychrometers similar to those used by Lourence and Pruitt (1969). These observations were made irregularly and data from these sensors were not used for any calculations.

In 1978, a more extensive network of temperature sensors was used to examine the development of the boundary layer over a snowpatch. Fourteen thermistor probes protected by radiation shields on four masts were erected on a large snowpatch approximately 300 m southeast of meteorological site 1 (fig. 2.1). The radiation shields were constructed of two offset concentric rings of plexiglass which formed the walls, and two circular styrofoam panels forming the top and the bottom (fig. 2.2). The external surfaces were then covered with highly reflectant mylar. This arrangement allowed the air to circulate past the thermistor while minimizing radiation heating on the sensor. This latter effect was noticeable only when there was no air movement to ventilate the shield. The temperatures measured by the thermistors were accurate to 0.1°C.



Approximate Scale  
10 mm = 25 mm



Top View (with top removed)

Fig. 2.2 Construction of the radiation shield used for the temperature sensors in 1978.

### 2.2.3. Wind

Wind speed was measured at 1 m above the snow with a Munro cup counting anemometer. Manual readings of the accumulated wind run were taken at irregular time intervals. To obtain hourly records, these readings were regressed against the 10 m wind speed measured hourly at the A.E.S. weather station (fig. 2.3).

The A.E.S. measurements are 1 minute averages obtained at the end of each hour. To make these values more comparable with those measured at the research site, a running mean was used to obtain average wind speed. As a result of the different methods by which the wind speeds were obtained, and the effect of a large hill, the scatter is large. The relationship between the study site ( $u_m$ ) and A.E.S. ( $U$ ) wind speeds

$$u_m = 0.572U + 0.96 \quad (2.1)$$

was used to estimate the mean hourly wind speed at the study site.

The surface roughness coefficient ( $z_0$ ) was obtained by taking simultaneous wind speed measurements using two anemometers positioned at 0.25 and 2.5 m above the snow. Roughness was then calculated for 15 minute periods, using equation (3.5). The mean surface roughness was 3.05 mm with a standard deviation of 1.73 mm. This value compares favourably with those obtained by Weller et al (1972) (2.5 mm), Lougeay (1974) (4.1 mm) for similar surfaces.

### 2.2.4 Other Meteorological Variables

Other meteorological information available from the A.E.S.

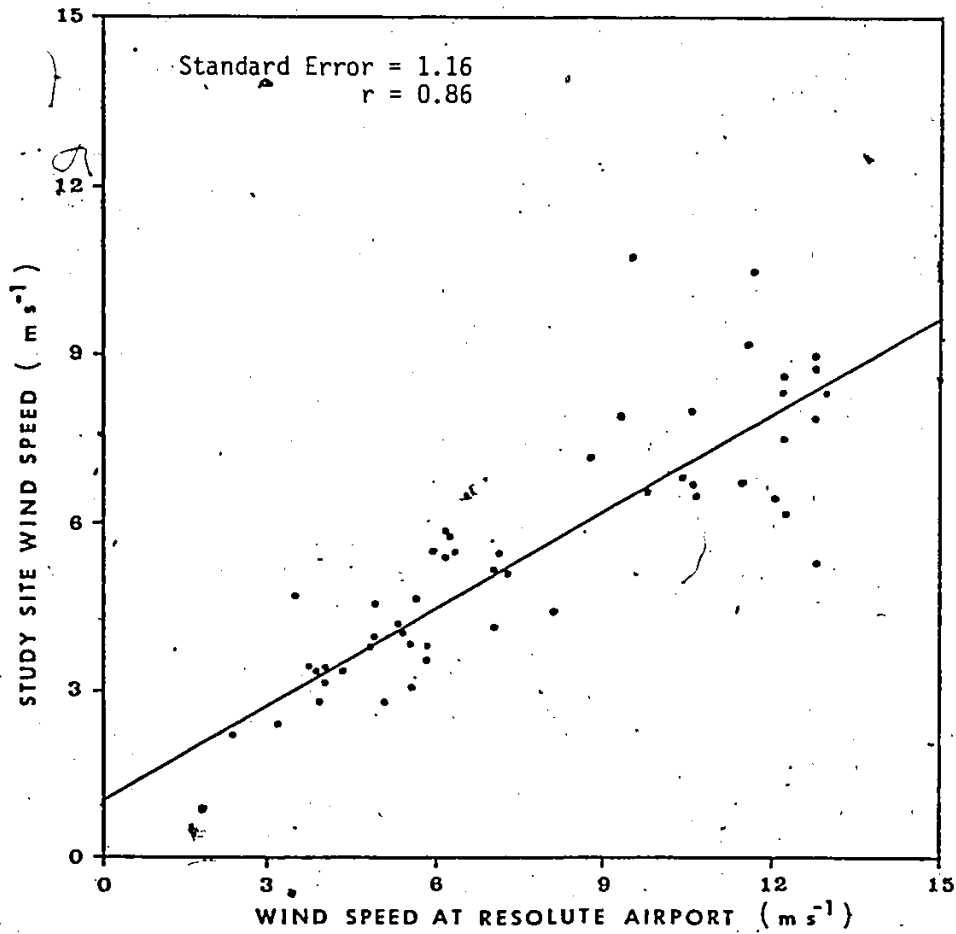


Fig. 2.3 Relationship between the 1 m wind speed at the study site and the 10 m wind speed at the Resolute Airport weather station.

weather office includes atmospheric air pressure, cloud cover information and precipitation. Precipitation was also measured at the research site, but only an insignificant amount of rain and snow was recorded in the study period.

## 2.2.5 Snow Measurements

### 2.2.5.1 Snow Ablation

To provide an independent check on the calculated surface energy balance, snow ablation was measured at several sites. Each measurement site consisted of a thin beaded wire held taut by springs and stretched between two stakes driven into the snow. The distance from the snowcover to the wire was measured to the nearest millimeter at each bead, and these distances were averaged. The amount of surface ablation (in water equivalent unit) was then obtained by

$$M = (h_{t+\Delta t} - h_t) / \rho_s \quad (2.2)$$

where  $h_t$  and  $h_{t+\Delta t}$  are the mean distances from the wire to the snow surface at time  $t$  and at time  $t+\Delta t$ , and  $\rho_s$  is the mean surface density of the snow during the time interval  $\Delta t$ .

The snow ablation was obtained on a nearly horizontal section of snow located to the south of the knoll shown in figure 2.1. In addition, ablation was also measured at sites on north (azimuth  $10^\circ$ ), east (azimuth  $135^\circ$ ), south (azimuth  $190^\circ$ ) and west (azimuth  $270^\circ$ ) facing slopes which had slope angles varying between  $8^\circ$  to  $15^\circ$ . Measurement

intervals varied between two and four hours during observation periods.

#### 2.2.5.2 Snow Density and Thermal Quality

To determine the snow surface density ( $\rho_s$ ) required by equation 2.2, 0.5 l snow cores were taken from the uppermost 0.08 m of the snow cover at each ablation site. These cores were weighed by a spring balance. Alternatively, snow density was obtained when the thermal quality is a measure of the moisture content of the snow. It is defined as

$$T = \lambda_a / \lambda_f \quad (2.3)$$

where  $\lambda_f$  is the latent heat of fusion and the apparent latent heat of fusion is

$$\lambda_a = (c_w (m_w + m_c) (\theta_i - \theta_f) - c_w m_s (\theta_f - 273)) / m_s \quad (2.4)$$

where  $c_w$  is the specific heat of water,  $m_w$  and  $m_s$  are the masses of warm water and snow,  $m_c$  is the water equivalent of the calorimeter,  $\theta_i$  and  $\theta_f$  are the initial and final water temperatures in the calorimeter in  $^{\circ}\text{K}$ .

The calorimeter used in this study consisted of a thermos flask with a temperature probe inserted through the lid and was simpler than those of Yosida (1966) and Leaf (1966). The accuracy of the calorimeters was approximately 5 percent. Because of the time involved, this latter procedure could be performed only once every three hours on the average.

### 2.2.5.3 Snowpack Temperatures

Snow temperatures were measured with thermistors at 0.25, 0.50, 0.75, 1.00 and 1.25 m above the ground-snow interface. Two thermistor arrays were installed, one at the north and the other at the southern site of the knoll. The resistance readings were measured daily, using a Lloyd resistance bridge accurate to 0.5 percent, and were converted to temperatures by an equation given by the manufacturer of the thermistors.



## CHAPTER THREE

### SNOWMELT AT A SITE

#### 3.1 Snowcover Conditions

In 1977, the snowpack began to ripen on steep southern slopes on June 2nd. At this time, the snow temperature was as low as  $-15^{\circ}\text{C}$  at the bottom of the pack (fig. 3.1). Latent heat was released to the surrounding snow as meltwater percolated from the snow surface and refroze in the pack, thus raising the temperature while creating ice lenses within the snowpack (fig. 3.2). These processes were accompanied by a decrease in the snowpack but an increase in the snow density caused by ice lense formation, a coarsening of the snow crystals and a higher water content. The surface thermal quality was approximately 93 percent, indicating that the snow had a 7 percent moisture content. At the base of the snowpack, the low density depth hoar crystals were replaced by an ice layer as energy was conducted to the underlying ground.

By June 10th, ripening was complete except for very deep packs. For very shallow packs, continuous melting led to the exposure of patches of bare ground (e.g., in the vicinity of meteorological site 1 and on the hilltops). These bare areas continued to grow until the end of June when only a few remnant snowpatches remained (fig. 3.3).

For the present study, only the energy exchange at the surface of the snowpack is considered. Heat exchange within the pack, although

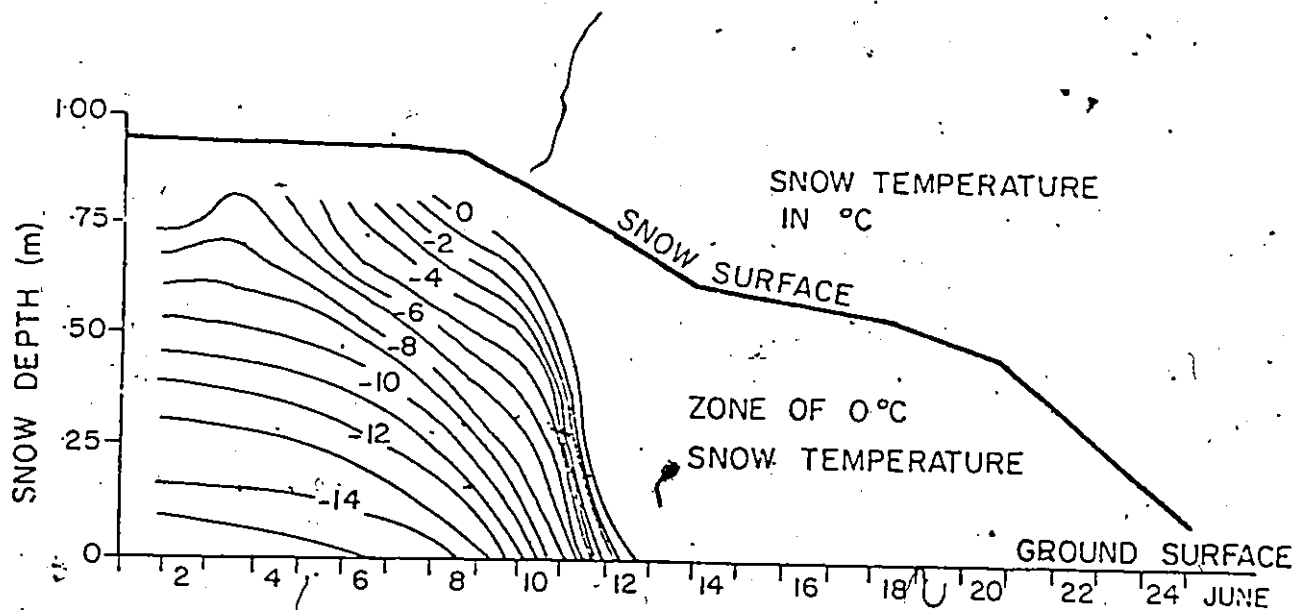


Fig. 3.1 Thermal regime of the snowcover before and during the study period.

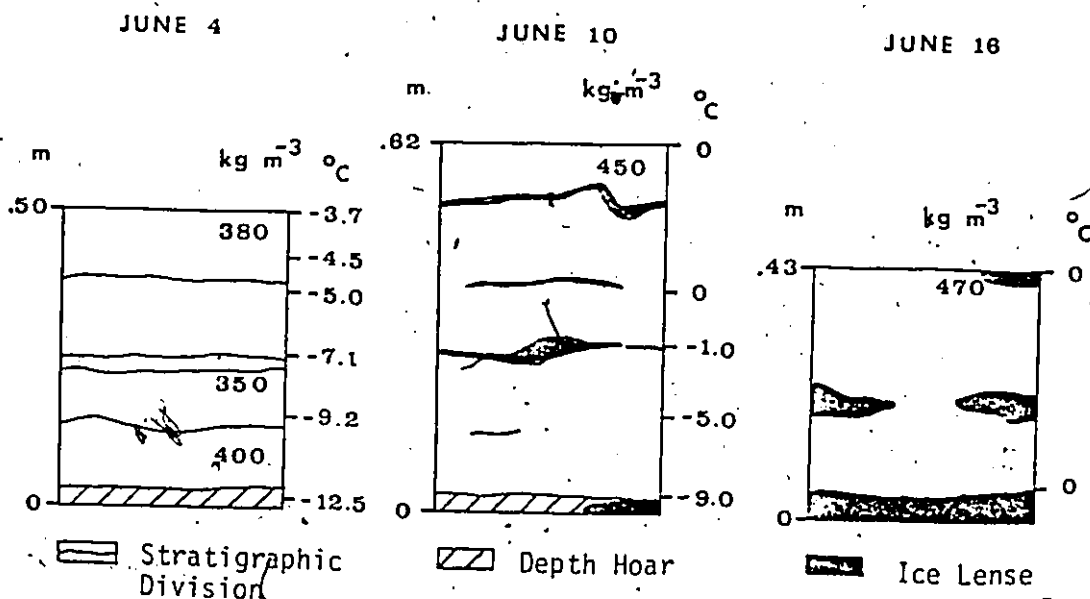


Fig. 3.2 Development of ice lenses in typical snowcover profiles.



Fig. 3.3 Spatial variation of the snowcover in the vicinity of the study site. The arrow points to meteorological site 1. The dates for these photos are June 8 (a), June 16 (b), June 20 (c), and June 29 (d).

important for such computations as meltwater release, is beyond the present scope of this study. However, the tendency of the Arctic snowpack to become patchy during the final phase of the melt period will affect the snow surface energy balance. In the sections to follow, the theory of snow surface energy exchange will be discussed and the field results will then be presented.

### 3.2 Surface Energy Balance Equation

At the surface of the snowpack, the energy balance is given by

$$Q_M = Q^* + Q_H + Q_E + Q_P \quad (3.1)$$

where  $Q_M$  is the energy available for melting,  $Q^*$ ,  $Q_H$  and  $Q_E$  are the fluxes of net radiation, sensible and latent heat. The energy added by precipitation is represented by  $Q_P$ . Ground heat flux was not considered in this study, but it is a term that should not be ignored if the energy balance of an entire pack is to be considered.

The terms on the right hand side of equation 3.1 must be calculated or measured in order to obtain the melt energy,  $Q_M$ . The net radiation flux can be readily measured with a net radiometer. The evaluation of the sensible and latent heat fluxes requires the measurement of temperature, humidity and wind speed at two or more levels above the surface. However, when the snow is melting, the surface temperature will be  $0^\circ\text{C}$  and the relative humidity, 100 percent. This permits the use of the bulk transfer approach to calculate fluxes from

$$Q_H = \rho_a c_p C_H u (\theta_z - \theta_s) \quad (3.2)$$

$$Q_E = \rho_a \lambda (\epsilon/P) C_E u (e_z - e_s) \quad (3.3)$$

where  $\theta_s$  and  $\theta_z$  are temperatures at the snow surface and at a height  $z$  metres above the surface,  $e_s$  and  $e_z$  the vapour pressures at the snow surface and at a height  $z$  metres above the surface,  $\rho_a$  the air density,  $c_p$  the heat capacity of air at a constant pressure,  $\lambda$  the latent heat of vapourization,  $\epsilon$  the ratio of the molecular weights of water and air,  $P$  the atmospheric pressure,  $u$  the wind speed at height  $z$ , and  $C_H$  and  $C_E$  dimensionless drag coefficients. Assuming that  $C_H = C_E = C_D$  and utilizing the logarithmic wind profile model,

$$C_D = k^2 / (\ln(z/z_0))^2 \quad (3.4)$$

where  $k$  is von Karman's constant.

The variable  $z_0$  is a measure of the surface roughness and can be estimated from wind speed measurements at two levels,  $z_2$  and  $z_1$  if a logarithmic profile is assumed,

$$z_0 = \exp\{(u_2 \ln z_1 - u_1 \ln z_2) / (u_2 - u_1)\} \quad (3.5)$$

The bulk transfer equations indicated above are valid only for neutral atmospheric conditions. To correct for the frequent occurrence of temperature inversions (stable equilibrium) over snow, the drag coefficient can be modified (Price et al 1976) using the Richardson number,  $Ri$ ,

$$Ri = gz (\theta_z - \theta_s) / \theta_z (u_z - u_s)^2 \quad (3.6)$$

where  $g$  is the acceleration due to gravity. For stable conditions ( $Ri > 0$ ), the drag coefficient is

$$C_{Ds} = C_D / (1 + \gamma Ri) \quad (3.7)$$

where  $\gamma$  is a coefficient with a value of 10 (Price et al 1976).

Unstable conditions are less common, but the drag coefficient can be modified by

$$C_{Du} = C_D / (1 - \gamma Ri) \quad (3.8)$$

Equations 3.2 to 3.8 have been derived to describe the energy exchange in the constant flux or boundary layer above a semi-infinite, rough, uniform surface. For these conditions to hold, it is assumed that the wind speed, temperature and humidity do not vary horizontally and that they are constant within the time interval considered. Under these conditions, only a vertical exchange of energy occurs. The above conditions occur over areas with large homogeneous surfaces, such as an extensive snowcover. However, during melt period, the snowcover breaks up and loses its homogeneity. This situation results in the formation of a poorly developed boundary layer as the air column moves from above the bare ground across the snow. Large horizontal temperature gradients may exist in this area of transition.

Weisman (1977) has investigated the thermal and humidity regimes of a boundary layer developed above a snowcover. His analysis indicates that when relatively warm and humid air moves over the snow, turbulent energy fluxes cause more rapid melting in a zone stretching approximately 20 m from the leading edge. With larger fetches, the turbulent energy fluxes decrease slowly as do the horizontal gradients of temperature and humidity. Although not derived for these conditions, one dimensional energy exchange equations 3.2 and 3.3 should provide an adequate estimate of the average energy exchange with the snowpack if the measurements are made near the center of the pack (Weisman 1977).

The remaining term of the energy balance, rain melt, can be evaluated by

$$Q_p = c_w \rho_w R(\theta_R - \theta_s) \quad (3.9)$$

where  $c_w$  is the specific heat of water,  $\rho_w$  the density of water,  $\theta_R$  the temperature of the rain, which can be approximated by the wet bulb temperature, and  $R$  the rainfall intensity.

When all the heat balance components are determined, the energy available for snowmelt,  $Q_M$  can be calculated by equation 3.1.

### 3.3 Computed Surface Energy Balance

Figure 3.4 summarizes the radiation and thermal regime for the snowmelt period. The most noticeable feature is the diurnal cycle in all of the variables, induced by daily variation in the short-wave energy.

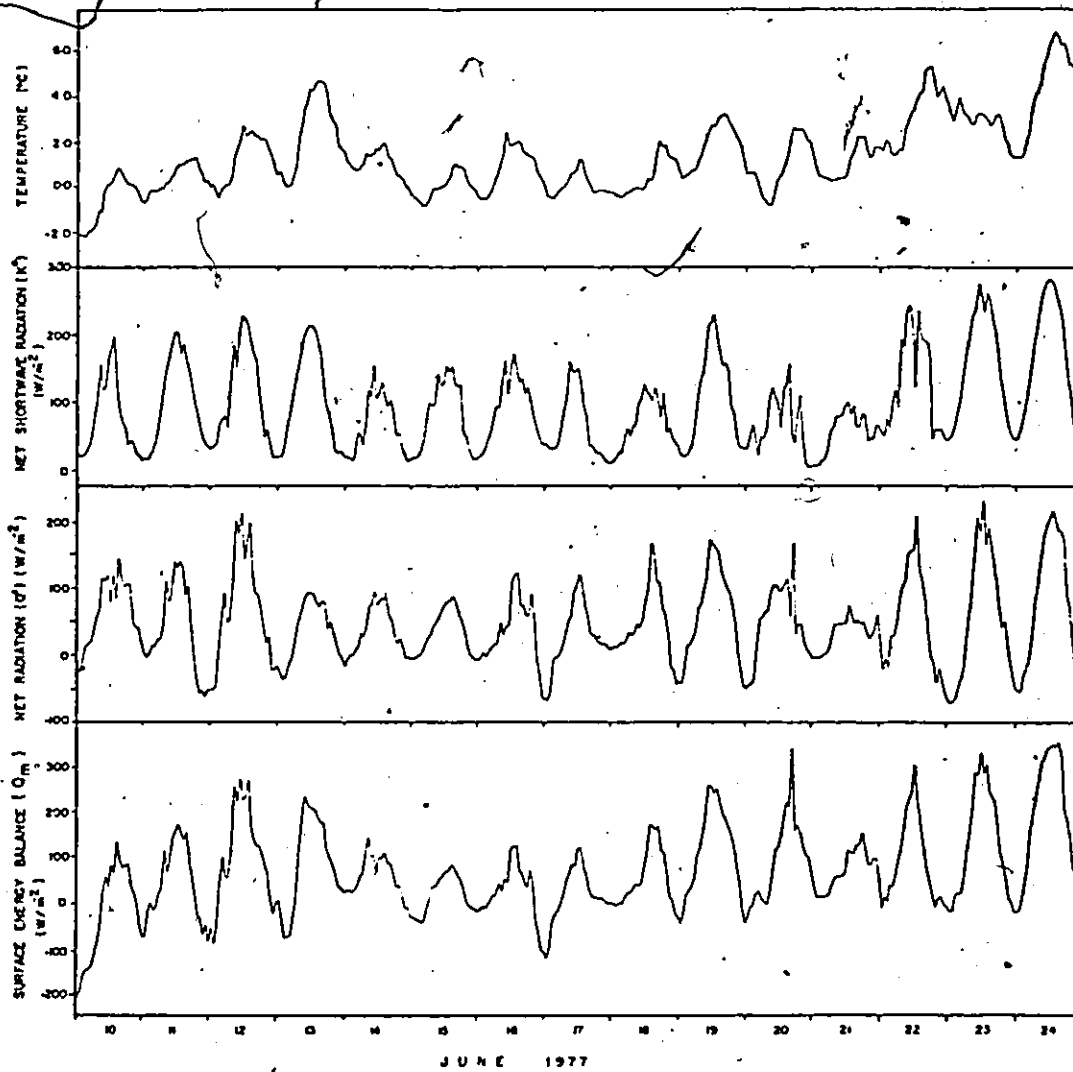


Fig. 3.4 Variation of air temperature, radiation and surface energy balance during the study period.



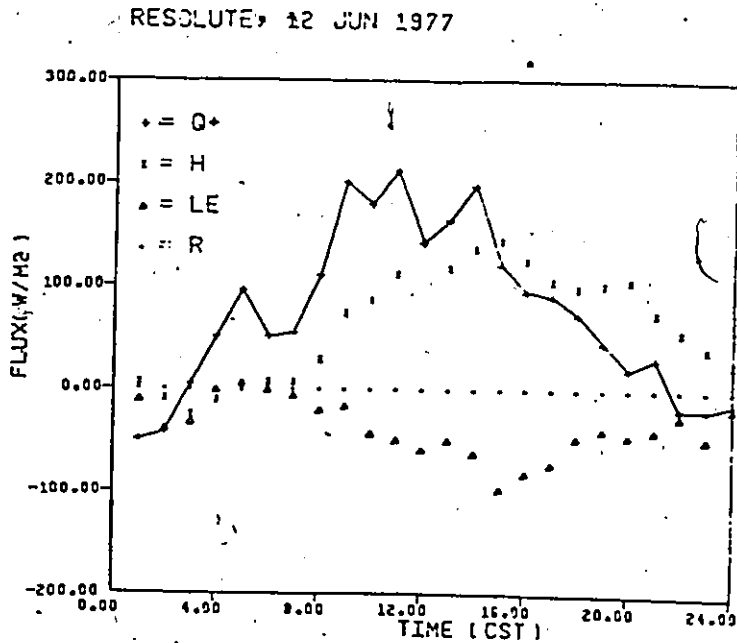
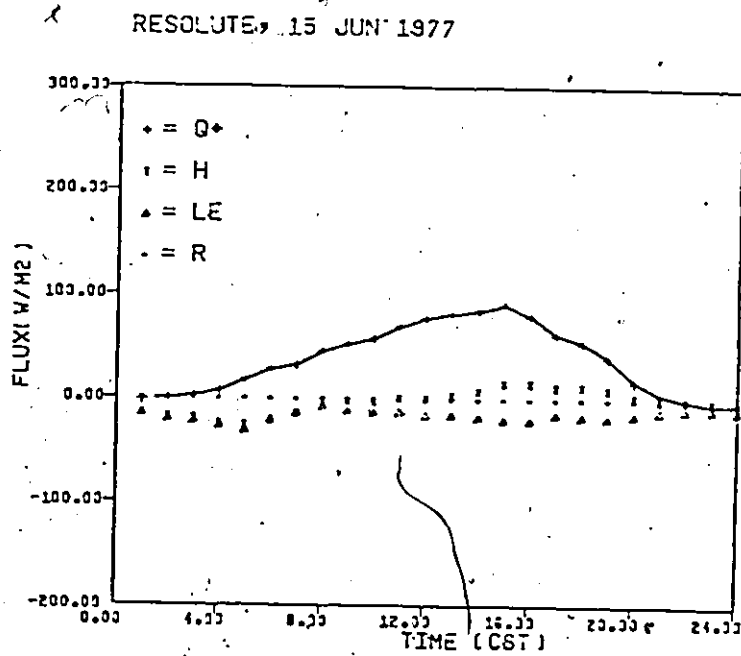


Fig. 3.5 Diurnal variation of the surface energy balance components during an overcast day (above) and a clear day (below).  $Q^*$  is the net radiation,  $H$  is the sensible heat flux,  $LE$  is the latent heat flux and  $R$  is the energy from precipitation.

Thus the amplitude of the diurnal cycle was greatest under a clear sky (June 10th to 13th) but was reduced when a cloud cover prevailed (June 14th to June 19th).

Figure 3.5 shows the hourly energy fluxes for a typical overcast day. Both net radiation and sensible heat fluxes were small. High humidity and near freezing temperatures produced low vapour pressure gradients and therefore a small latent heat flux. The resulting surface energy balance was small. There was no negative net radiation, but a period of surface energy loss occurred during the early morning and late evening.

On a clear day with scattered clouds (June 12th), the net radiation component was much larger than on June 15th. However, five hours of negative net radiation were measured when the sun was low in the sky. Sensible heat flux was large, peaking three hours after the net radiation maximum. Both the sensible and latent heat fluxes produced prominent diurnal cycles which tended to mirror each other. The cause of these 'mirror images', which also occurred June 14th, 16th and 17th (Appendix 1), is not known, but may be due to bare ground upwind affecting the moisture content of the air or possibly the result of instrumental error. No patterns similar to these were described in the literature.

The various components of the energy balance were partitioned on a daily basis for the entire study period. Although drizzle occurred in the melt period, it contributed little energy to melting and has been ignored in figure 3.6. The heat flux to the snow is then the sum of the

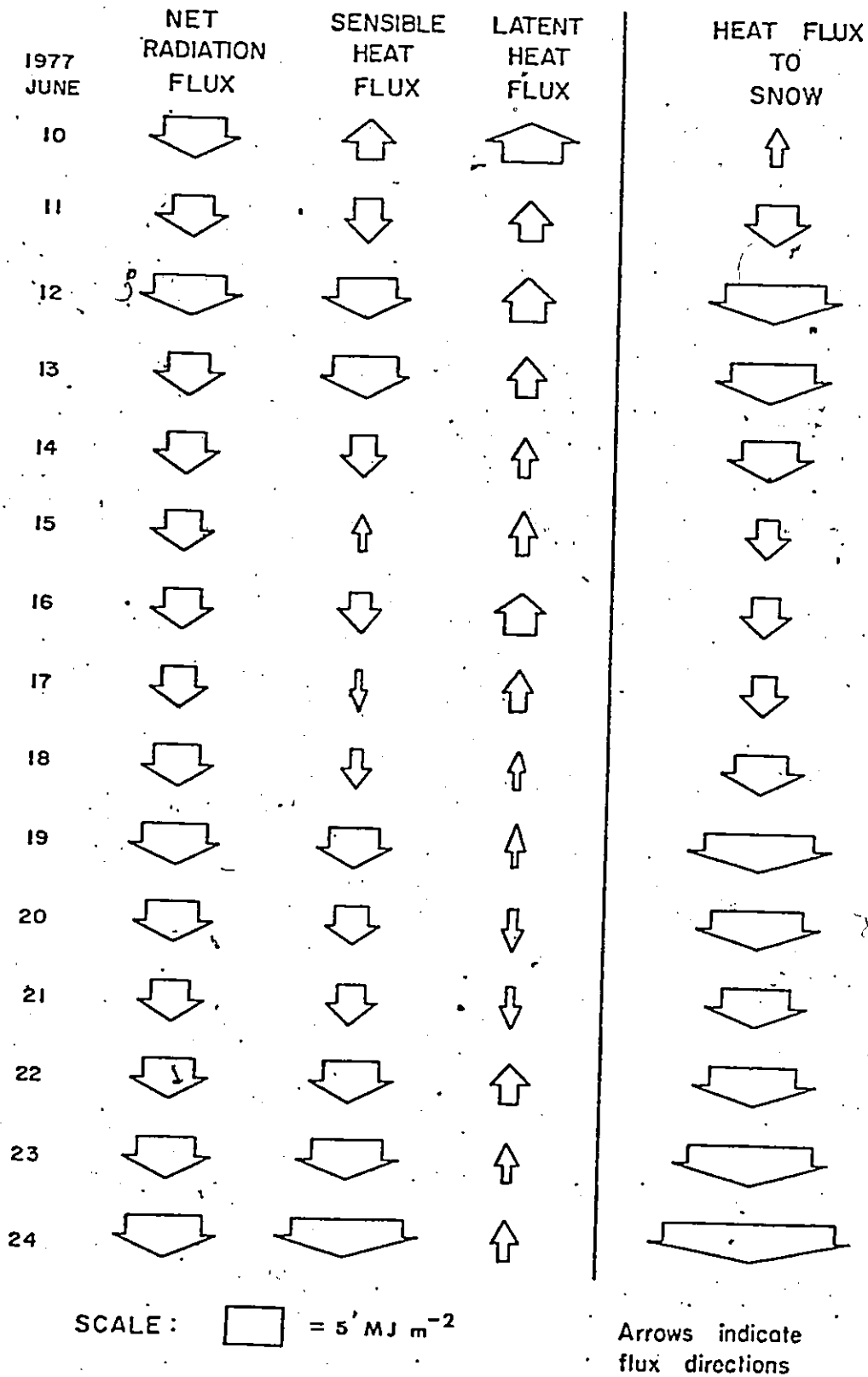


Fig. 3.6 Daily variation of the energy balance components. The width of the arrow indicates the relative magnitude of the energy fluxes.

TABLE 3.1

## DAILY TOTALS OF THE SURFACE ENERGY BALANCE COMPONENTS AND DAILY ABLATION

Date	Energy Balance Components				Ablation	
	$Q^*$	$Q_H$	$Q_E$	$Q_M$	Calculated	Observed
	MJ m <sup>-2</sup> day <sup>-1</sup>				mm day <sup>-1</sup>	mm day <sup>-1</sup>
June 10	5.6	-2.6	-5.2	2.2	-6.2 (7.8*)	7.3*
11	3.2	2.3	-2.0	-3.6	10.7	26.7
12	6.5	5.6	-3.2	-8.8	26.3	37.9
13	3.3	5.9	-1.7	-7.5	22.4	20.0
14	3.3	2.6	-1.0	-5.0	14.8	17.2
15	3.2	-0.3	-1.4	-1.5	4.6	12.5
16	3.2	1.8	-3.1	-1.9	5.7	10.9
17	2.9	0.1	-1.4	-1.6	4.7	10.3
18	4.1	0.9	-0.3	-4.7	14.0	12.1
19	5.6	4.6	-0.3	-9.9	29.5	31.0
20	4.7	3.1	0.5	-8.3	24.9	22.5
21	3.2	2.6	0.4	-6.2	18.5	23.7
22	4.5	5.0	-1.9	-7.6	22.9	33.0
23	5.6	6.5	-0.9	-11.3	33.7	20.0
24	6.9	9.9	-1.2	-15.6	46.6	30.3

\* 1000 h to 2400 h

net radiation, sensible heat and latent heat components. Figure 3.6 and table 3.1 indicate that during the overcast and foggy days in the middle of the melt period the energy available for melt was reduced. For the rest of the melt period, accelerated melt was primarily due to an increase in the sensible heat gained by the snow, although the net radiation component also increased. The flux of latent heat removed a large amount of energy early in the melt period, but as the air warmed and its moisture content increased, the energy loss decreased. Latent heat provided energy for snowmelt on only two occasions.

Over the entire measurement period, net radiation accounted for 58 percent of the total energy input to the snow while 42 percent was contributed by sensible heat. Eighty percent of the energy received was used for snowmelt and the remaining 20 percent was consumed in evaporation.

#### 3.4 Comparison of Calculated, and Measured Values

Snow ablation at a site was measured as an independent check on the calculated energy balance. Figure 3.7 compares the cumulative measured and calculated ablation values. This graph was obtained by accumulating the hourly calculated melt and evaporation values and superimposing the resulting curve on a plot of the observed ablation. The fit is very good but the calculated values under estimate the observed values by 9 percent. Figure 3.7 and table 3.1 indicate that there are several periods with poor comparisons. One occurred during the first three days of the study period when the snowpack was not completely ripe as shown by the fact that the pack was not yet isothermal at  $0^{\circ}\text{C}$  (fig. 3.1). The

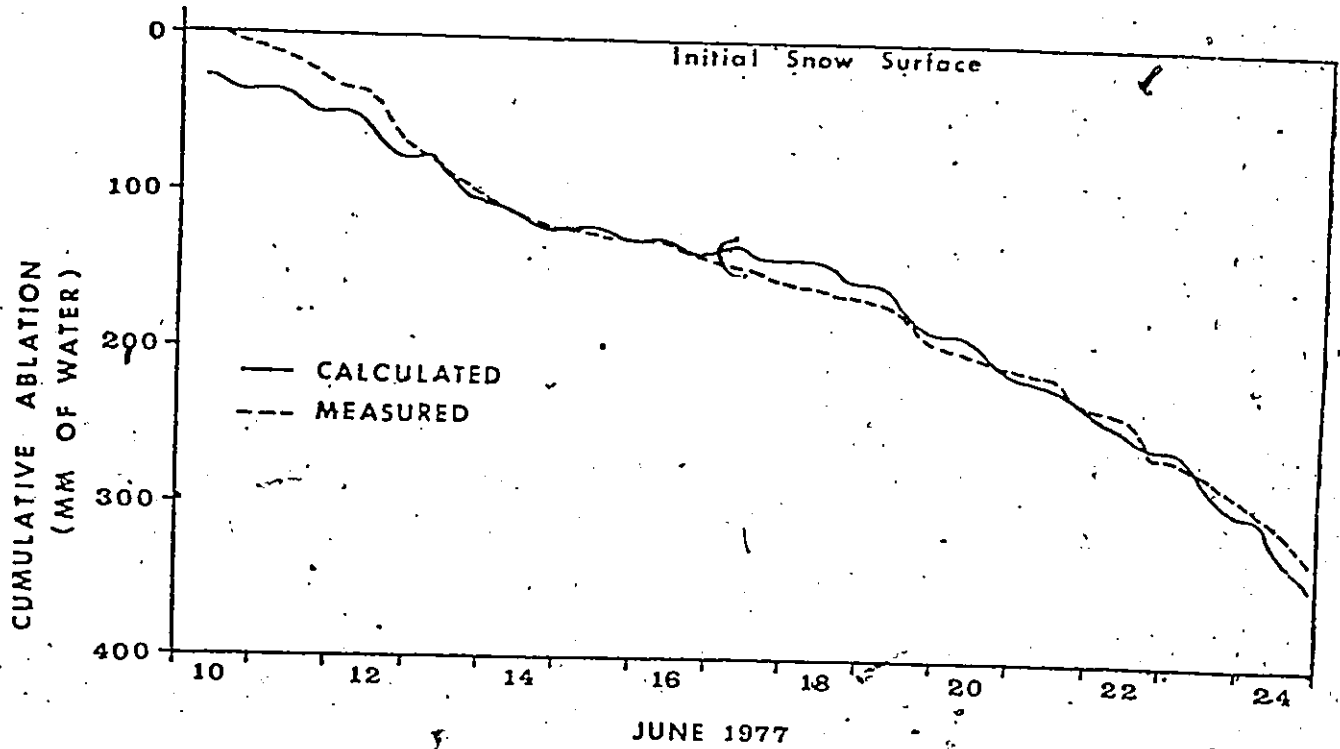


Fig. 3.7 Comparison of cumulative calculated snowmelt and cumulative measured ablation.

calculated values are also in error on the first day. Some data were missing in the early morning and the estimated values indicated that no melt should have occurred. However, melt was observed, so no calculated values prior to the start of the ablation measurements were used.

A second period of disagreement occurred from June 15th to 17th when overcast conditions prevailed. Light drizzle fell but the intensity was not measurable and may have caused an under estimation of the rain melt. Also for part of the period, the wind speed at the study site was higher than equation 2.1 indicated and would result in an under estimation of the melt.

The third period with discrepancies occurred when extensive areas of bare ground produced an advection of sensible heat to the snow-patch. This was particularly prominent after June 22nd when the snow-patch was so reduced in extent that the meteorological readings at 1 m were probably not representative of the boundary layer over the snow. Approximately 20 mm of melt should have occurred on each of the final two days of the melt period, but twice that value was computed.

This last example is shown more clearly in figure 3.8 where the daily values of calculated ablation are plotted against measured. The scatter in this plot is rather large. This is due in part to the need to interpolate the measured ablation between the last observation on one day and the first of the following day. However, the points which have large over estimates of the melt occurred late in the melt period while the large under estimates happened early.

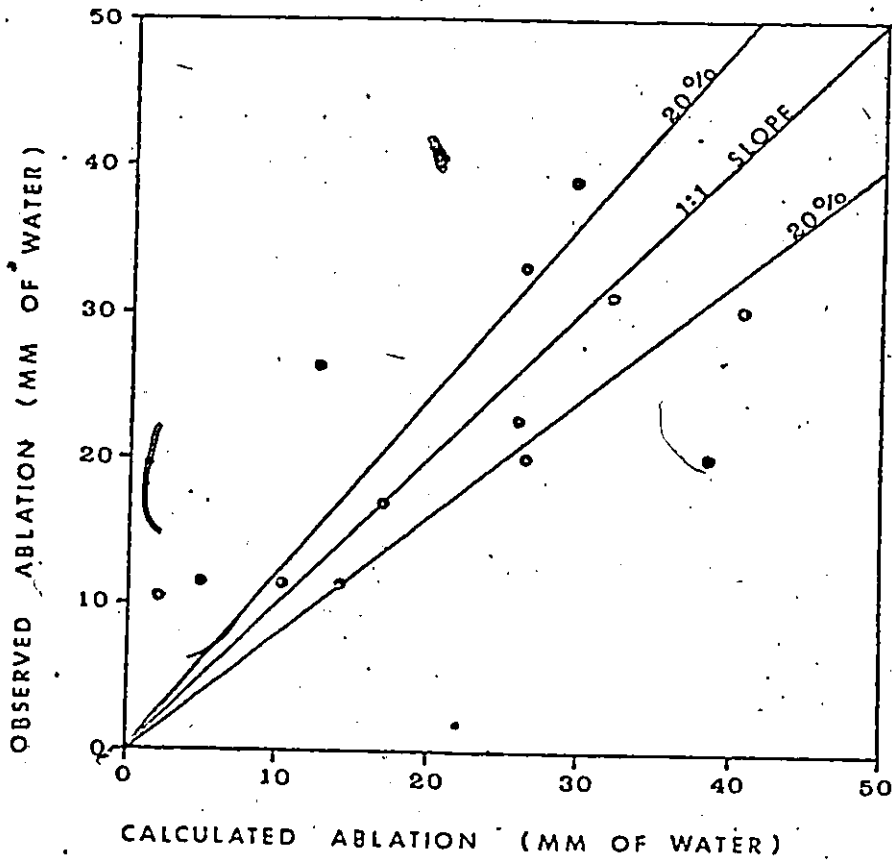


Fig. 3.8 Comparison of daily calculated snowmelt and daily observation ablation.



### 3.5 Development of the Boundary Layer

During mid-days towards the end of the study period, bare ground adjacent to the study site was a source of warm air which was advected to the snowpack. As noted in section 3.2, an accurate evaluation of sensible and latent heat fluxes is contingent upon the condition that pertinent meteorological variables are measured in the boundary layer immediately above the snowpack. This requires a better appreciation of the manner in which the boundary layer develops from the leading edge towards the center of the pack.

In 1978, some observations were made in this regard. Two examples are shown in fig. 3.9. In these diagrams, the wind is from the left and the apparent top of the boundary layer is indicated with a dashed line. In both cases, temperature inversions existed over the snow and large horizontal temperature gradients developed. The initial temperature profiles were different. On July 14th, the initial vertical temperature profile showed a normal lapse condition. The boundary layer developed rapidly once the leading edge of the snow was traversed. For July 15th, the initial profile was more complex, being affected by a variable wind speed crossing another snowpatch approximately 20 m upwind.

These two examples demonstrate that in the period when the snowcover was patchy, the temperature, humidity and wind sensors have to be sufficiently far from the leading edge or they should be sufficiently low to be within the boundary layer. An examination of the 1977 temperature data for elevations of 1 and 2 m above the snow where the fetch was less than 20 m (fig. 3.10) indicates that the upper level is clearly

Height  
above snow  
(m)

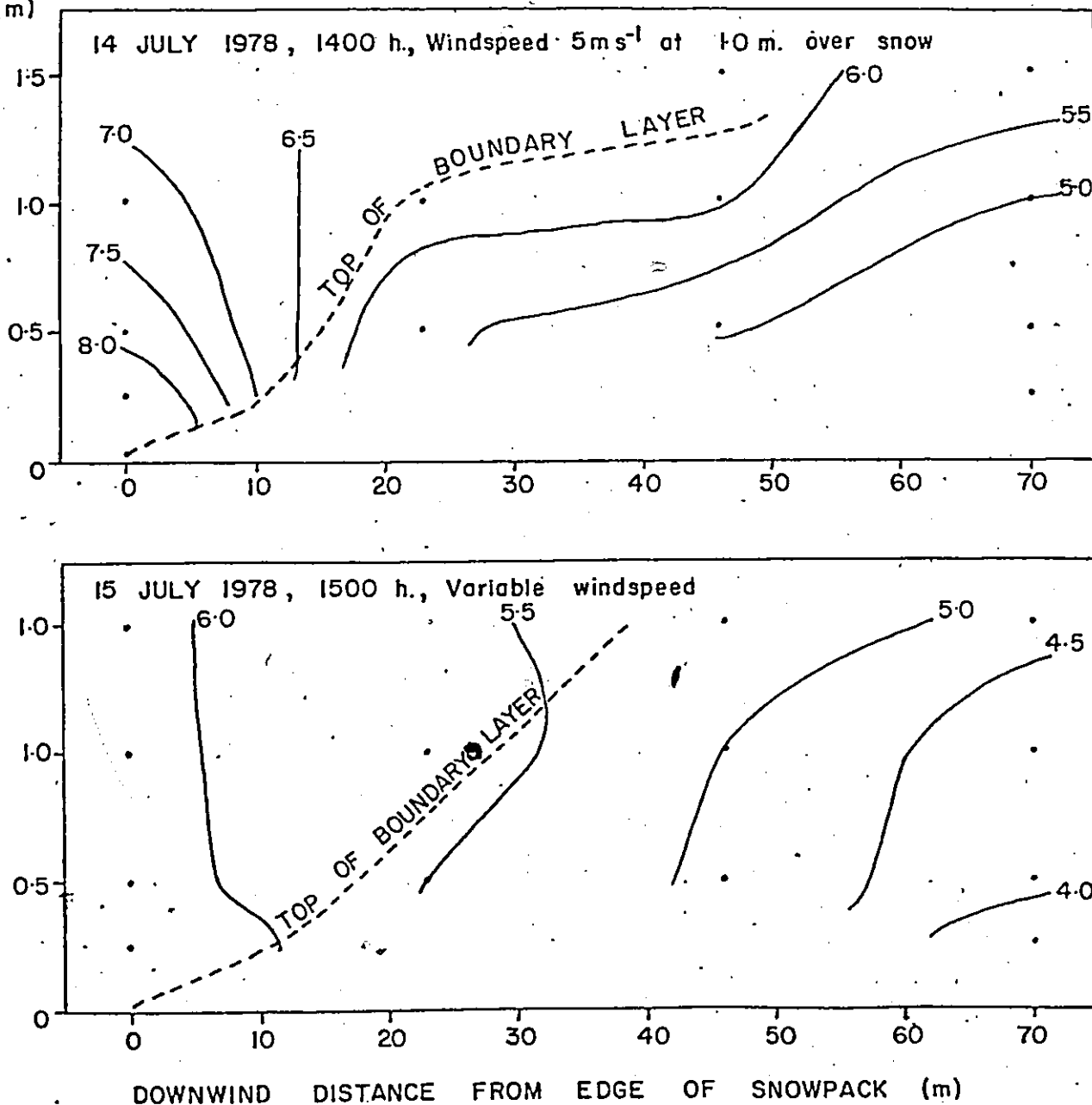


Fig. 3.9 Temperature profiles above part of a snow patch showing development of a boundary layer as air is advected from left to right of the diagrams. The dots indicate the location of temperature measurement and the isotherms are in  $^{\circ}\text{C}$ .

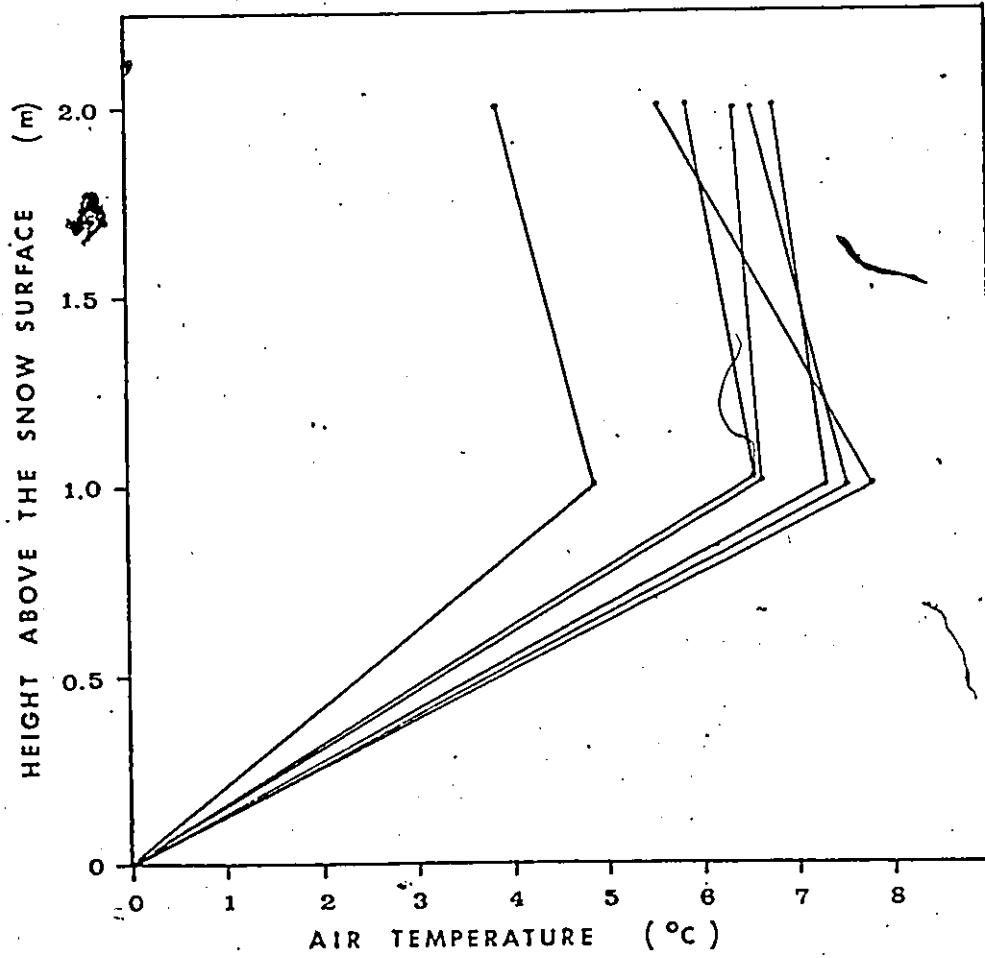


Fig. 3.10 Air temperature profiles over the snow surface on June 24, 1977.

outside the boundary layer and when combined with the 1978 data suggests that the lower level was outside as well. In this case, observations from the 1 m level would yield an over estimation of the sensible heat flux and possibly account for the substantial difference between the predicted and observed amount of snowmelt for the last few days of the study period. However, earlier in the melt period, the snowcover was more continuous and the 1978 experiment implies that the fetch was sufficient for a boundary layer to be well developed to a height of 1 m where measurements were taken.

### 3.6 Comparison with Results from Other Studies

Snow and ice melt studies have been conducted in different locations and under a wide variety of conditions. To place the results of the present study in the context of the others, Table 3.2 summarizes the findings of selected studies. These studies are separated into five groups on the basis of their study location.

In the present study, net radiation accounted for approximately 60 percent of the incoming energy while the flux of sensible heat supplied the remainder. This finding compares favourably with the majority of the studies cited, but is different from the results from other Arctic tundra sites, some of the Prairie sites and from several other locations.

At the tundra sites, while net radiation supplied all of the incoming energy, sensible and latent heat were both energy losses. Although the reasons for our differences are not entirely clear, some of

TABLE 3.2 SUMMARY OF PREVIOUS ENERGY BALANCE STUDIES

Study	Location	Site	Q*	Energy Balance Components				
				Q <sub>H</sub>	Q <sub>E</sub>	Q <sub>M</sub>	Other	
	<u>Arctic Tundra</u>							
Ohmura (1972)	Axel Hieberg Is. 1969	Snow	100	-26	-49	-25	-	
Ohmura and Muller (1976)	Axel Hieberg Is. 1970	Snow	100	-12	-15	-53	-20	
Weller et al (1974)	Barrow, Alaska 1971	Snow	100	-18.7	N.A.	-59.7	-21.6	
Present Study	Cornwallis Is. 1977	Snow	58	42	-20	-80	-	
	<u>Other Arctic Locations</u>							
Lister (1962)	Ellesmere Ice Shelf	Ice	96	4	-4	N.A.	-	
Müller and Keeler (1969)	White Glacier 1961	Ice	56	43	0.5	-80	-19.5	
	1962	Ice	66	28	6	-88	-12	
(from Lougeay (1974))	Sverdrup Glacier 1962	Ice	53	32	15	N.A.	N.A.	
	1963	Ice	51	34	15	N.A.	N.A.	
Orvig (1954)	Barnes Icecap 1950	Snow	67.7	32.3	-	N.A.	-	
	Penny Icecap 1953	Snow	61.3	8.8	29.9	-100	-	
Wendler et al (1973)	McCall Glacier	Ice	69.7	29.9	.4	-98.7	-1.3	
	<u>Sub-Arctic</u>							
Price (1977)	Schefferville 1973	Snow	46	54	-7.5	-92.5	-	
Wendler (1967)	Fairbanks 1966	Snow	86	14	-24	-76	-	

Study	Location	Site	Q*	Q <sub>H</sub>	Q <sub>E</sub>	Q <sub>M</sub>	Other
Granger and Male (1977)	<u>Prairies</u> Saskatchewan 1974 1975 1976	Snow	59	41	-14	-86	-
		Snow	95	5	-22	-78	-
		Snow	54	46	-15	-58	-27
O'Neill (1972)	Saskatchewan	Snow	93	7	N.A.	N.A.	-
		Snowpatch	56	44	N.A.	N.A.	-
Aufdemberge (1974)	<u>Other Locations</u> Capps Glacier	Ice	80.4	12.2	7.2	-100	.2
		Snowpatch	29	71	N.A.	N.A.	-
Cox and Zuzel (1976)	Alps	Snowfield	85	15	-15	-85	-
De la Casiniere (1974)	Alps	Snow	56	44	-3	-97	-
De Walle and Meiman (1971)	Alpine Clearing	Snow	44	48	8	-100	-
Föhn (1973)	Peyto Glacier	Snow	75	25	-74	-26	-
Gold and Williams (1960)	Ottawa, Ontario	Snow	69	25	6	-100	-
La Chapelle (1959)	Blue Glacier	Snow	99.8	.2	-1.1	-98.9	-
Lougeay (1974)	Seward Glacier 1965	Snow	51	29	20	-100	-
Streten and Wendler (1968)	Worthington Glacier	Ice					

NOTE: 1) All values are expressed as a percentage of the incoming (+ ve) energy.  
 2) The energy balance component 'other' includes the ground heat flux, rain melt, energy storage and balancing error.  
 3) N.A. means information not available.

the possible explanations will be examined. Weller et al (1972, 1974) examined the surface energy balance during the snowmelt period at Barrow, Alaska. They recorded a positive daily mean air temperature for a substantial part of the melt period. However, sensible heat was an energy source for only a few days. This flux was obtained using mean daily temperatures and gradients obtained from two levels above the surface. If at least one measurement level had been outside the boundary layer a temperature gradient directed away from the surface may have yielded a negative flux. The lowest measurements were 0.5, 1, and 2 m and fig. 3.9 indicates that if the fetch was not adequate, one or more levels could have been outside the boundary layer. The snowcover was complete only at the beginning of the melt period when positive sensible heat fluxes were obtained. Although positive air temperatures continued, the sensible heat flux became negative. The bare ground that existed from the middle of the melt period onwards may have disturbed the boundary layer in the vicinity of the sensors. For the entire melt period, the information presented by Weller et al (1972, 1974) suggests that the flux of sensible heat should contribute more energy than indicated.

Little information is available to enable an initial examination of the results of Ohmura and Müller (1976), though additional information was given in Ohmura (1972). Like Weller et al (1972), positive daily mean air temperatures and negative sensible fluxes are reported. With this temperature regime over a melting snow surface, a positive sensible heat flux is expected. Ohmura also reported that the temperature regime in the lower atmosphere was an inversion while the

temperatures of the air layers in contact with the ground indicated a lapse condition. This observation contradicts the common experience that a temperature inversion is expected when both snow and positive air temperatures are present. Hence, his results suggest an advection of warm air from nearby bare ground and the temperature readings were not representative of the zone within the snow boundary layer.

The above discussion indicates the results from the snowmelt period of these three studies should be treated with caution. Information provided by these papers suggests that the flux of sensible heat should be a heat source rather than an energy loss. If this is true, then net radiation could not have supplied all the snowmelt energy.

In terms of snowmelt in the Prairie (environment, most studies) were conducted over complete snowcover. In some years, net radiation provided almost all of the snowmelt energy. Such results are not directly comparable to those of the present study. This study was limited to the period when the snow pack was ripe while the former also included the snow ripening period.

The Prairie snow studies also showed that in certain years the net radiation and sensible heat components were of comparable magnitudes. In these cases, air masses were responsible for high air temperatures (Granger 1977). Of particular relevance to the present study is the result of O'Neill (1973) obtained over a snowpatch in the Prairies. Our findings are comparable, with net radiation and sensible heat accounting for 56 and 44 percent of the incoming energy while those of the present study are 58 and 42 percent respectively.



For the other studies listed in table 3.2, the net radiative flux provided approximately 50 to 90 percent of the incoming energy depending upon the local atmospheric conditions. An exception is the study of Cox and Zuzel (1976) which was performed over a snowpatch. Their study demonstrated that advected energy can provide an important source of energy for snowmelt.

## CHAPTER FOUR

### SNOWMELT ON SLOPES

#### 4.1 Introduction

In the preceding chapter, the surface energy balance at a site was investigated. However, snowmelt can be expected to vary spatially. To estimate the snowmelt for a catchment or other extended and non-homogeneous area, an estimate of the spatial variation with the surface energy balance is required. Snowmelt is known to vary with slope angle and slope aspect. Assuming that the fluxes of sensible ( $Q_H$ ) and latent ( $Q_E$ ) heat are the same for both the horizontal site and neighbouring slopes, then the energy available for snowmelt on a slope ( $Q_{Msl}$ ) can be calculated as

$$Q_{Msl} = Q_{sl}^* + Q_H + Q_E + Q_P \quad (4.1)$$

where  $Q_{sl}^*$  is the net radiation balance of the slope,  $Q_H$  and  $Q_E$  the fluxes of sensible and latent heat at a horizontal site and  $Q_P$  the heat contributed by precipitation.

#### 4.2 Calculation of the Radiation Balance of Slopes

##### 4.2.1 Net Radiation on Slopes

The radiation balance of a horizontal surface can be defined

as

$$Q^* = K_{\downarrow} - K_{\uparrow} + L_{\downarrow} - L_{\uparrow} \quad (4.2)$$

where  $Q^*$  is the net radiation of the surface,  $K_{\downarrow}$  the incoming flux of short-wave radiation,  $K_{\uparrow}$  the flux of short-wave radiation reflected from the surface,  $L_{\downarrow}$  the flux of long-wave radiation from the atmosphere and  $L_{\uparrow}$  the long-wave radiation flux emitted from the surface. On a non-horizontal surface several additional sources of radiant energy should be taken into account. Normally, these sources are small, but in certain situations, they may become important. As given by Kondratyev (1969) the net radiative flux to a slope is

$$Q_{s1}^* = I_{s1} + D_{s1} + R_{s1} - K_{\uparrow s1} + L_{\downarrow s1} + L_{rh} + L_{eh} + L_{\uparrow s1} \quad (4.3)$$

where  $I_{s1}$  is the incoming direct short-wave radiation,  $D_{s1}$  the diffuse short wave radiation,  $R_{s1}$  the short-wave radiation reflected to the slope,  $K_{\uparrow s1}$  the short wave radiation reflected from the slope,  $L_{\downarrow s1}$  the atmospheric long-wave radiation received by the slope,  $L_{rh}$  the long-wave radiation reflected to the slope,  $L_{eh}$  the long-wave radiation emitted from adjoining surfaces to the slope and  $L_{\uparrow s1}$  the long-wave radiation emitted by the slope.

Equation 4.3 can be used to calculate the net radiative flux to a slope if the radiation balance components for a horizontal surface are known.

#### 4.2.2 Direct Short-Wave Radiation

The direct short-wave radiation flux is the most important component of the radiation balance of a slope. Since short-wave radiation arrives directly from the Sun, the magnitude of the energy received on a slope from this source is dependent upon the time of year, the time of day, the slope angle and azimuth and the atmospheric conditions.

Garnier and Ohmura (1968) have indicated that the flux of direct short-wave radiation on a slope is

$$I_{sl} = I_0 p^m \cos i \quad (4.4)$$

where  $I_0$  is the solar constant,  $p$  the atmospheric transmissivity,  $m$  the optical air mass and  $i$  the angle of incidence between the slope perpendicular and the Sun. Using finite intervals approximation, total incident direct short-wave radiation over a period ( $n\Delta t$ ) can be written

$$I_{sl} = (I_0/r^2) \sum_{j=1}^n p^{m_j} \cos(i_j) \Delta t \quad (4.5)$$

where  $r$  is the radius vector of the Earth's orbit and  $t$  is the time interval. The inclusion of  $r^{-2}$  in the equations enables an adjustment of the solar constant according to the distance between the Earth and the Sun. The cosine of the angle of incidence is given by Williams et al (1972) as

$$\cos i = (c_1 \sin H + c_2 \cos H + c_3) \quad (4.6)$$

where H is the hour angle of the Sun, being negative before noon and positive after noon. When  $\cos i < 0$  then the slope would receive no direct short-wave radiation.

$$c_1 = -\sin A \sin S \cos \phi \quad (4.7)$$

$$c_2 = (\cos \phi \cos S - \sin \phi \cos A \sin S) \cos \zeta \quad (4.8)$$

$$c_3 = (\sin \phi \cos S + \cos \phi \cos A \sin S) \sin \zeta \quad (4.9)$$

where A is the azimuth (eastward from north) S the slope angle,  $\phi$  the latitude and  $\zeta$  the solar declination.

To make the scheme operational, the solar declination (in radians) is

$$\zeta = \sin^{-1} \{ .39785 (4.868961 + .017203 d + .033446 \sin(6224111 + .017202 d)) \} \quad (4.10)$$

where d is the Julian date. This equation produces declinations accurate to  $0.5^\circ$  and requires only the Julian date (Swift 1976).

Williams et al (1972) give the radius vector of the Earth's orbit as

$$r = 0.01676 \cos (\pi - 0.0172615 (d - 3)) + 1 \quad (4.11)$$

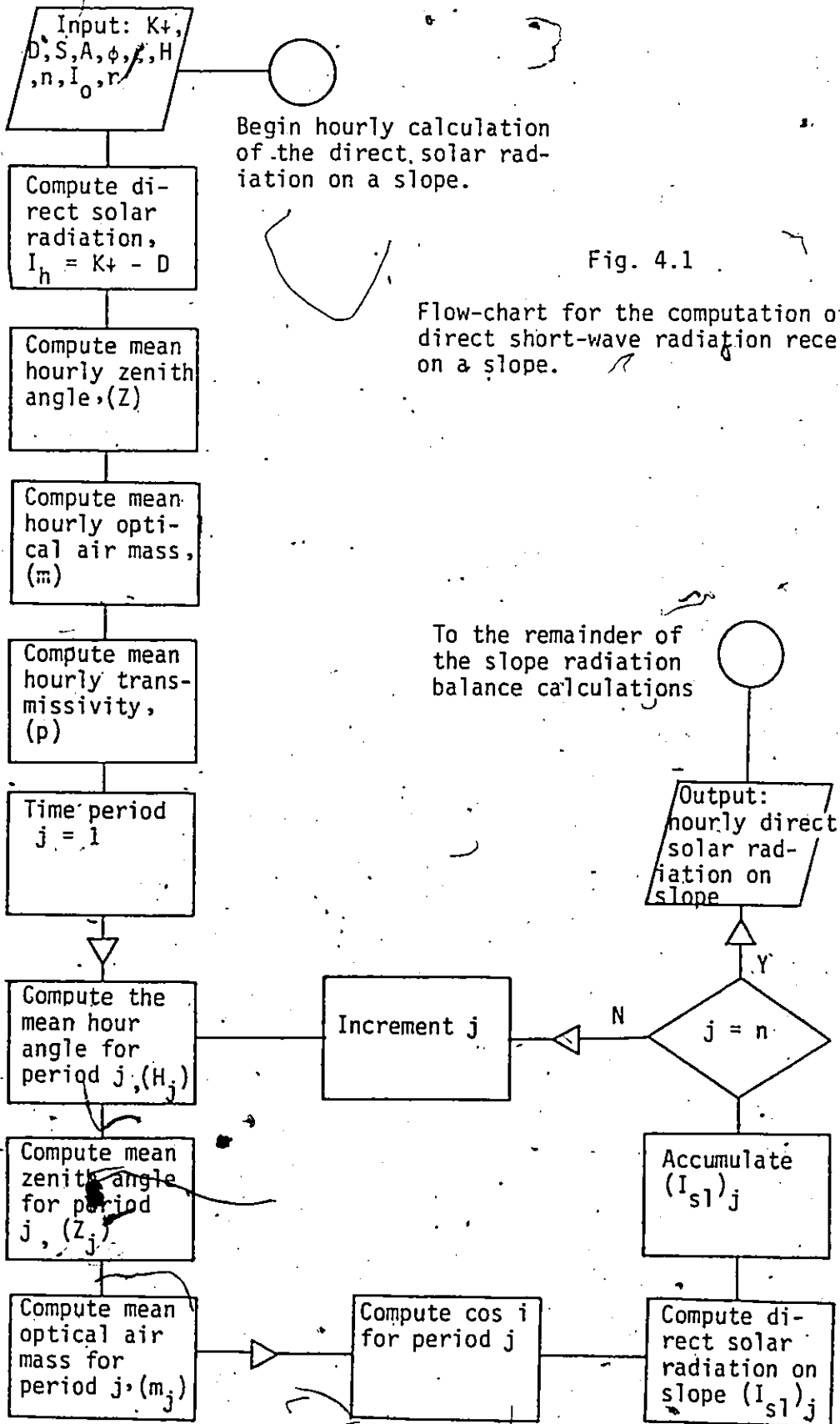


Fig. 4.1

Flow-chart for the computation of direct short-wave radiation received on a slope.

The optical air mass required in equation 4.5 can be expressed as-

$$m = \{(R_e \cos Z)^2 + 2R_e + 1\}^{0.5} - R_e \cos Z \quad (4.12)$$

where  $R_e$  is the ratio of the radius of the Earth to the thickness of the atmosphere and  $Z$  is the solar zenith angle. The optical air mass can be approximated by  $m = \sec Z$ , but the formula used here is more accurate at large zenith angles. The cosine of the zenith angle can be calculated from

$$\cos Z = \cos \zeta \cos \phi \cos H + \sin \zeta \sin \phi \quad (4.13)$$

where  $\zeta$  is the solar declination,  $\phi$  the latitude and  $H$  the hour angle.

The incident direct short-wave radiation on a slope was calculated using equations 4.6 to 4.13 and the logic provided by figure 4.1. The mean hourly transmissivity ( $p$ ) was obtained from equation 4.4 by replacing  $i$  and  $I_S$  with the mean zenith angle and the direct short-wave radiation received on a horizontal surface

$$I_h = Kt - D \quad (4.14)$$

where  $D$  is the diffuse radiation received at a horizontal site. The mean hourly transmissivity was then used to calculate the incident short-wave radiation off a slope for smaller time periods from equation 4.5. In this study, the measurement period ( $n\Delta t$ ) was one hour and the time interval ( $\Delta t$ ) was 15 minutes. Garnier and Ohmura (1970) indicated that a 20 minute time interval produced cumulative incident short-wave totals that were

within 5 percent of those using a 1 minute interval.

#### 4.2.3 Diffuse Short-wave Radiation

Diffuse short-wave radiation results when direct solar radiation interacts with clouds and other particles in the atmosphere. Numerous reflections and refractions occur which result in the radiation approaching the surface from all points in the sky. In overcast conditions, the scattering is so severe that no direct radiation reaches the ground surface and the diffuse radiation becomes isotropic. In clear conditions, little scattering occurs and the diffuse radiation is not isotropic.

The diffuse radiation received on a slope is

$$D_{s1} = D \cos^2 (S/2) \quad (4.15)$$

where  $D$  is the amount of diffuse radiation measured on a horizontal surface and  $S$  the slope angle. Equation 4.14 assumes that the incoming diffuse radiation is isotropic. This is a reasonable assumption for overcast conditions but is not valid when there is little or no cloud cover. However, when the latter conditions prevail, the amount of diffuse radiation will be small when compared to the direct short-wave radiation.

#### 4.2.4 Reflected Short-wave Radiation

The third input of short-wave radiation is reflection from the adjacent slopes. Assuming that reflected radiation is isotropic, the



short-wave radiation reflected to a slope is

$$R_{sl} = \alpha_h K \sin^2(\theta/2) \quad (4.16)$$

where  $K$  is the short-wave radiation received on a horizontal plane with an albedo  $\alpha_h$ .

The short-wave radiation loss from a slope is given by

$$K_{sl} = \alpha_{sl} (I_{sl} + D_{sl} + R_{sl}) \quad (4.17)$$

where  $\alpha_{sl}$  is the albedo of the slope. Evidently, the accuracy of equations 4.15 and 4.16 depend upon the albedo of the surface.

During the melt period, snow surface albedo can decrease from 0.8 to 0.5 or less as the snow ripens. The dependence of albedo on zenith angle adds diurnal cycles to the general trend of albedo decline. Albedo also varies with cloud cover, surface moisture and other surface conditions. Taking some of the above variables into account, Petzold (1977) developed a model to predict snow albedos. While the seasonal decay and the effect of cloud cover were isolated, the variation due to the zenith angle could not be easily predicted. For surfaces other than snow, Arnfield (1975) modelled the surface albedo ( $\alpha$ ) using

$$\alpha = f_1 \exp(f_2 Z) \quad (4.18)$$

where  $Z$  is the zenith angle and  $f_1$  and  $f_2$  were empirically determined

from regression analysis. Equation 4.18 did not perform well for snow: instead, the following equation will be used in this study

$$\alpha = \{1/((E/a) + b_1)/b_2 + \alpha_0 \quad (4.19)$$

where  $E$  is the solar elevation,  $\alpha_0$  the snow albedo at high solar elevations, and  $a, b_1, b_2$  are empirical coefficients. To obtain snow albedo for slopes, the solar elevation above the slope can be substituted in equation 4.19 for the solar elevation above a horizontal surface. The solar elevation above the slope is  $90 - i$ , where  $i$  is the angle of incidence of the Sun's rays on the slope and can be obtained from equation 4.7.

#### 4.2.5 Long-wave Radiation

Net long-wave radiation can be measured, but is usually obtained from

$$L^* = Q^* - (K\downarrow - K\uparrow) \quad (4.20)$$

The flux of long-wave radiation emitted can be calculated if the surface temperature is known and is given by the Stefan-Boltzman equation

$$L\uparrow = \delta \sigma \theta_s^4 \quad (4.21)$$

where  $\delta$  is the emissivity of the surface,  $\sigma$  the Stefan-Boltzman constant and  $\theta_s$  the surface temperature. Thus, the long-wave radiation

arriving at the surface from the atmosphere is the residual

$$L_{\downarrow} = L^* - L_{\uparrow} \quad (4.22)$$

Following equation 4.15 and assuming an isotropic distribution of the incoming long-wave radiation, the atmospheric long-wave radiation received by a slope is

$$L_{\downarrow S1} = L_{\downarrow} \cos^2(S/2) \quad (4.23)$$

There are two other long-wave fluxes that may contribute energy to a slope. One is the flux of long-wave radiation reflected from adjoining slopes

$$L_{rh} = (1 - \delta) L_{\downarrow} \sin^2(S/2) \quad (4.24)$$

This flux is small since  $\delta \approx 0.97$  (Kondratyev 1969). The other flux is the receipt of radiation emitted from the adjacent slopes and is given by

$$L_{eh} = \delta \sigma \theta_s^4 \sin^2(S/2) \quad (4.25)$$

To complete the long-wave energy balance for a slope, the emitted radiation ( $L_{\uparrow S1}$ ) will be given by equation 4.21, assuming that the surface temperatures are equal.

### 4.3 Results

#### 4.3.1 Albedo

The importance of snow surface albedo is shown by equation 4.17. The albedo during the melt period was obtained using a hand held pyranometer at the net radiometer site and at some of the snow ablation sites. Radiometer malfunctions reduced the data, but sufficient data remained to indicate the seasonal decay rate (fig. 4.2)

$$\alpha_0 = -0.0060 J + .679 \quad (4.26)$$

where J is the number of days since June 7th. However, more frequent manual readings of the albedo of semi-permanent snowpatches obtained after the study period indicated that a strong diurnal variation existed. The data obtained in this manner was not adequate to model the diurnal cycles.

The weather station at Resolute measures both incident and reflected short-wave radiation, thus permitting the surface albedo to be computed. From its data, several clear days, when the snow could be expected to be melting, were chosen to derive the empirical coefficients for equation 4.19. The results for one of these days is shown in figure 4.3. The value of  $\alpha_0$  was estimated from the minimum albedo values and the curve was fitted by eye. The values used for the coefficients  $a$ ,  $b_2$  and  $b_1$  in equation 4.19 were 10, 10 and 0.4 respectively. Since at this time of the year, the sun rises more than  $40^\circ$  above the horizon or never sets, equation 4.19 cannot be applied with certainty to those slopes with a larger range in solar elevation.

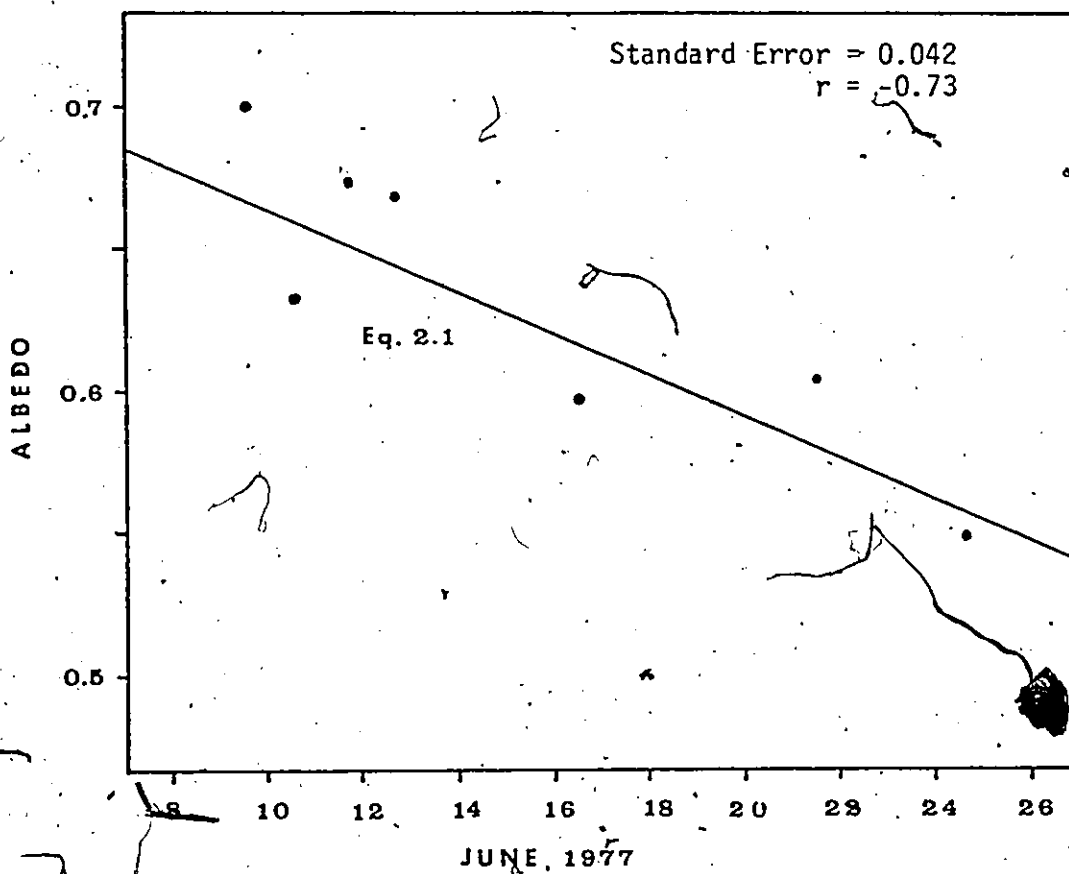


Fig. 4.2 Decay of the snow surface albedo during the study period.

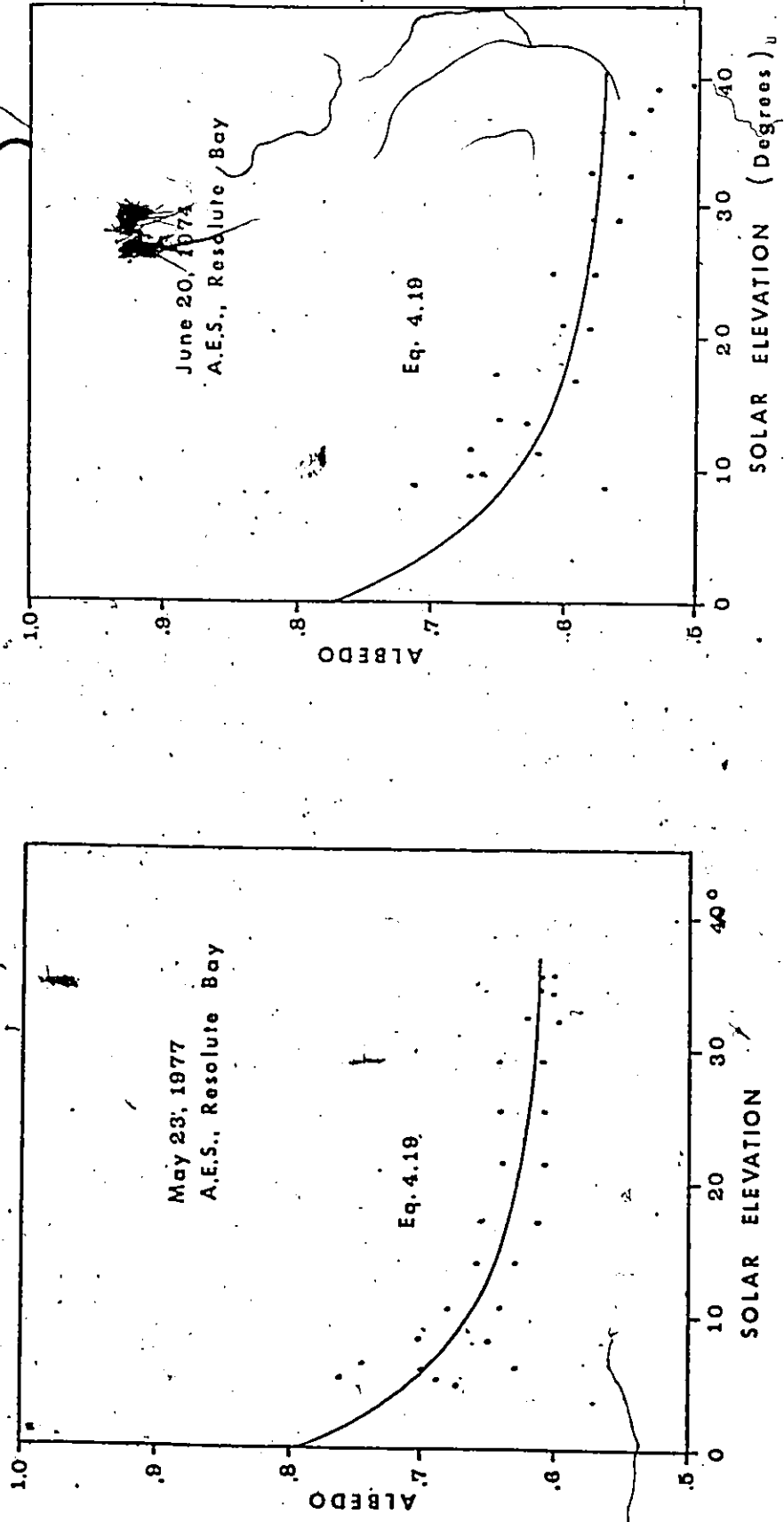


Fig. 4.3 Relationship between solar elevation and snow albedo measured by the Atmospheric Environment Service at Resolute Bay.

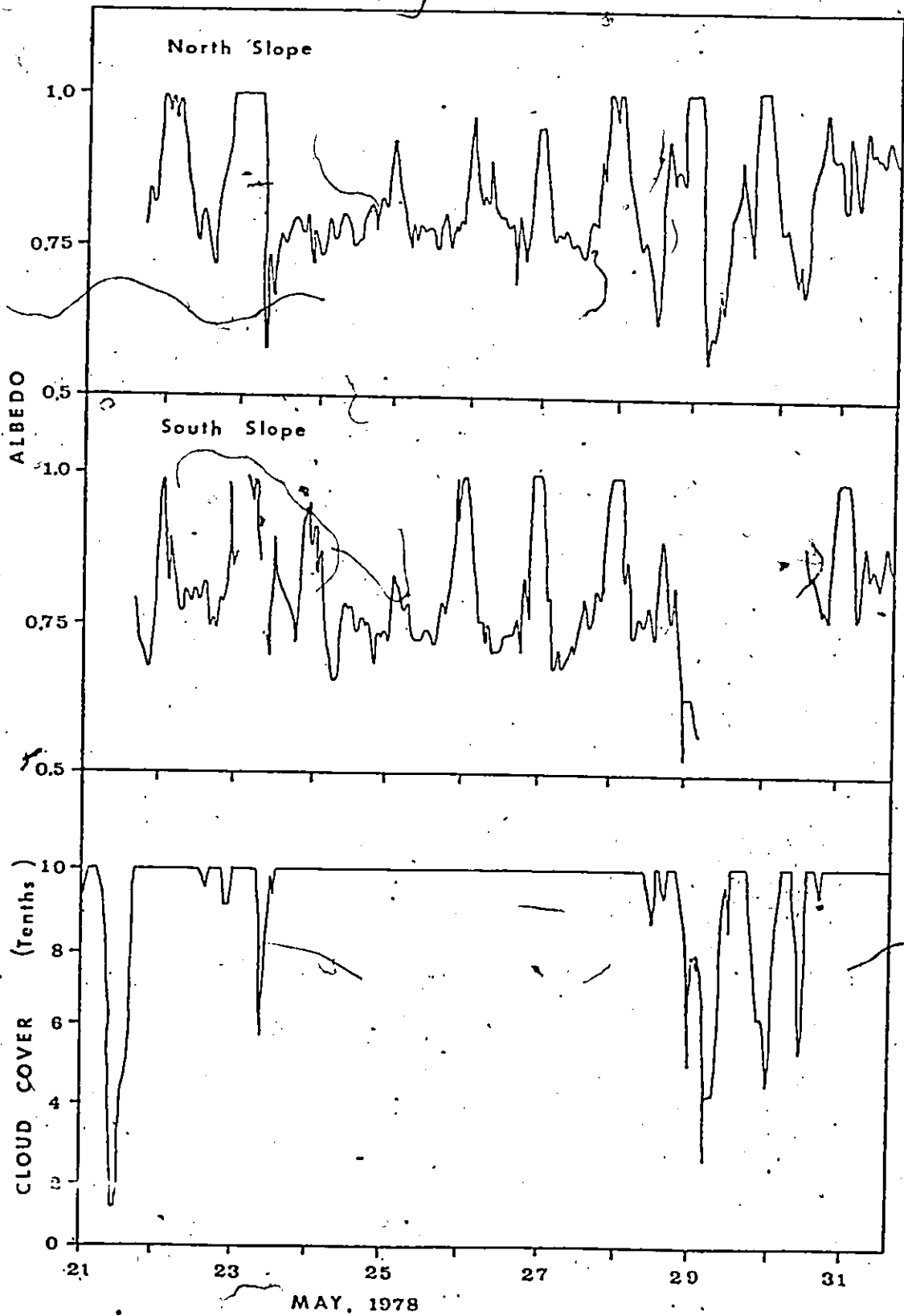


Fig. 4.4 Diurnal variation of albedo on north and south slopes during an overcast period.

In an attempt to correct this lack of information, the snow surface albedo was calculated for north and south of  $16^{\circ}$  slopes in 1978. The reflected short-wave radiation was measured and the albedo on the slope was calculated from

$$\alpha_{sl} = K_{sl} / (I_{sl} + D_{sl} + R_{sl}) \quad (4.27)$$

using equations 4.5, 4.15 and 4.16 and A.E.S. data for direct and diffuse solar radiation. The results presented in figure 4.4 were obtained during a predominantly overcast period. Diurnal cycles are visible on both slopes and this result contrasts with the findings of Hubley (1955) that the albedo on an overcast day did not vary greatly or in a systematic manner. The snow albedo obtained for a horizontal site later in 1978 also shows diurnal cycles under complete cloud cover (fig. 4.5). At all three sites, the snow was not melting so that the diurnal cycle can not be attributed to surface changes. For the north and south slopes, figure 4.6 indicates that the snow albedo varies inversely with the solar elevation above the horizontal but not the solar elevation above the slope. The reasons for the relationship between albedo and solar elevation above the horizontal when the sky is overcast are not clear. The shade ring on the diffuse solar radiation sensor was not adjusted correctly for part of the albedo measurement period, so it is possible that the slopes received more direct radiation than was calculated. This by itself would not produce the diurnal cycles, but would affect the calculations of the incident solar radiation. The reflection of short-wave radiation to the slope from those adjacent was not included in equation 4.27 and could have been



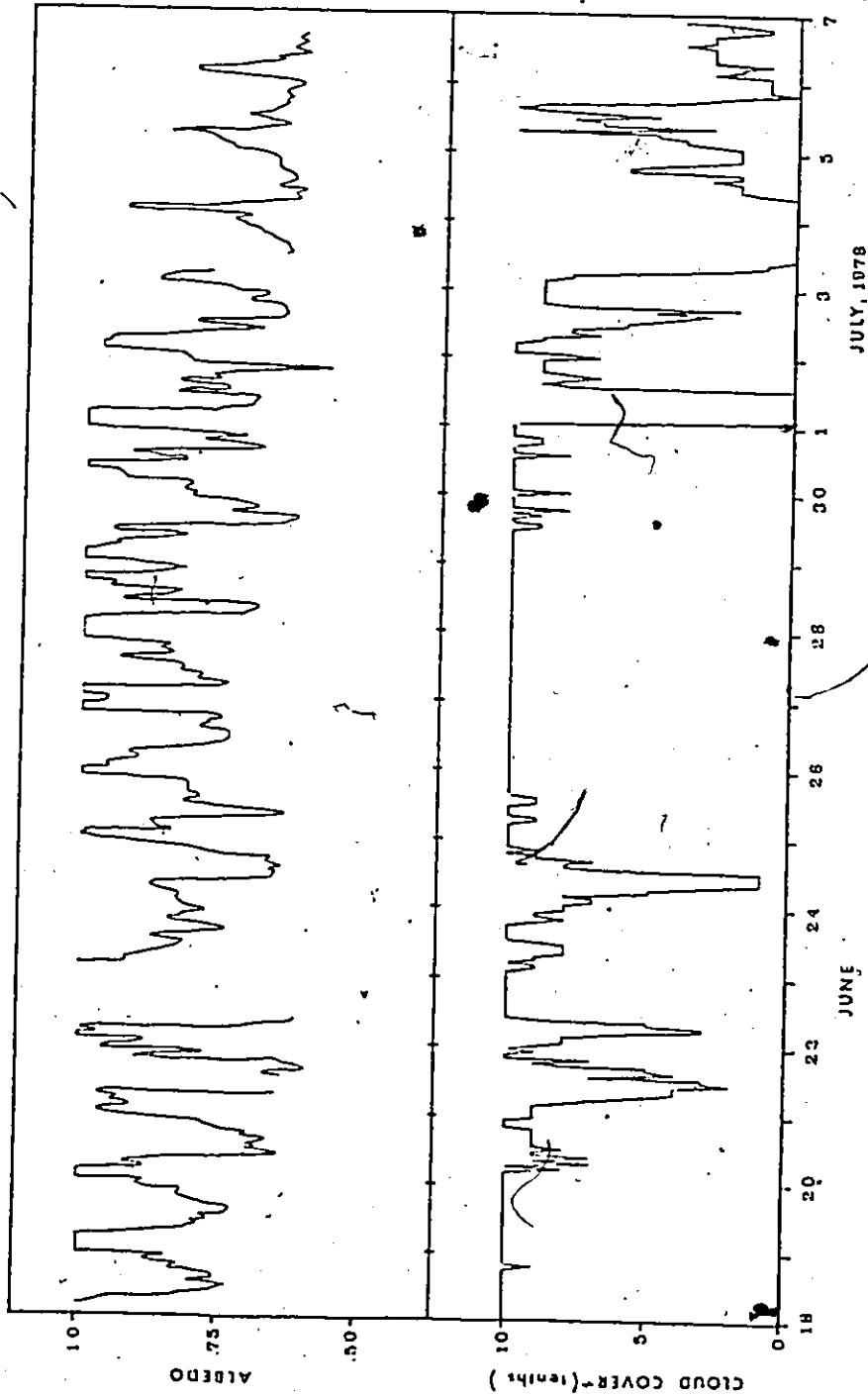


Fig. 4.5 Cloud cover and diurnal variation of albedo on a horizontal surface.

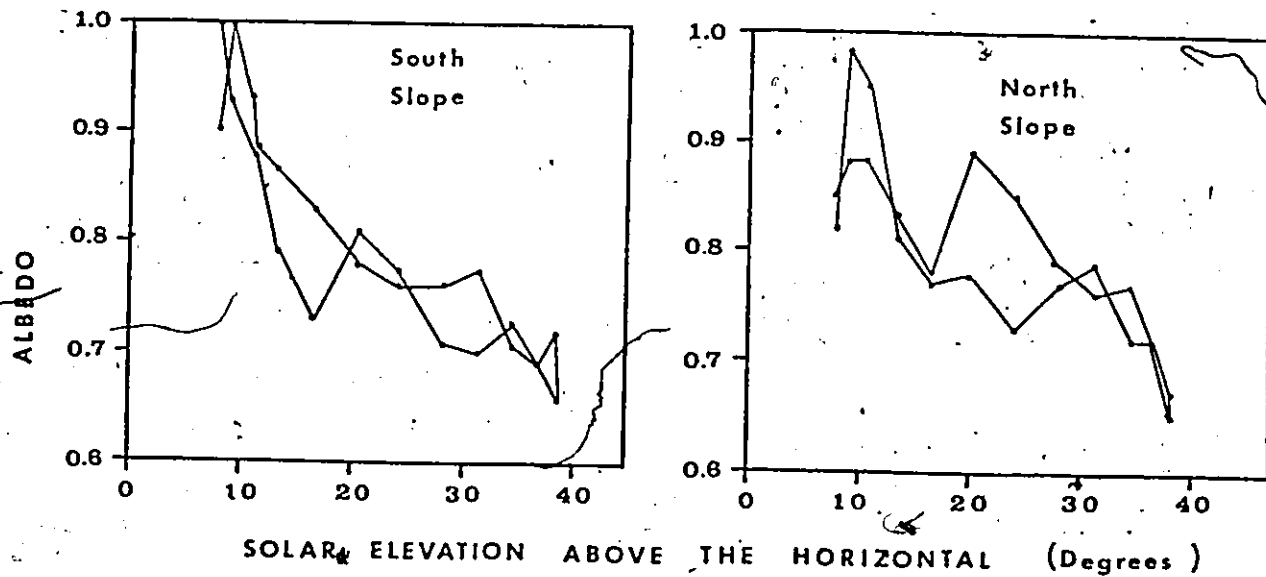
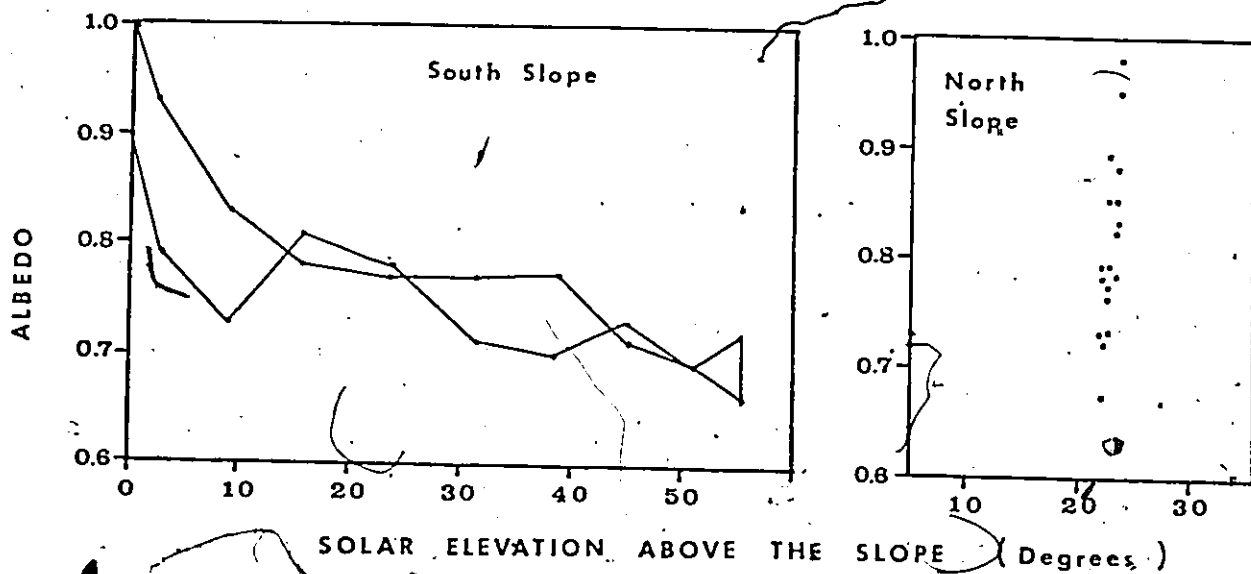


Fig. 4.6 Relationship between albedo and solar elevation above the slope and horizontal, June 11, 1978.

partly responsible for the diurnal cycles on the slopes.

The behaviour of the snow albedo on slopes when the sky was clear cannot be verified with the data obtained since the diffuse radiometer shield was not correctly located at these times.

Based upon the above information four conditions for the calculation of albedo are identified. For skies with an incomplete cloud cover, the solar elevation above a horizontal surface was replaced with the solar elevation above the slope and equation 4.19 was used. For thin cloud covers, the slope albedo was equal to the albedo on the horizontal as calculated by equation 4.19. Under more cloudy conditions and when fog was present, a constant albedo was assumed. The final condition occurred only when the slope was in shadow; that is, it was receiving no direct radiation while the surrounding areas were. The albedo under this condition was assumed to be .75. The south slope was in shadow approximately 6 hours each night, and the results suggest that the snow albedo increases. Aufdenberge (1974) suggests that the albedo decreases when shading occurs while Petzold (1977) indicates that albedo increases when diffuse radiation is the only incident short-wave radiation. The albedo value chosen above is a compromise between these results.

The inconsistency of the results of this study compared to those from other studies indicates that additional theoretical work (Giddings and La Chapelle 1963) and field measurements are required to obtain more accurate predictions of the variation of snow albedo with both time and space.

#### 4.3.2 Slope Radiation Balance on Clear Days

Using the procedures outlined in sections 4.1 and 4.2, the net radiation balances for 12 slopes were calculated for a relatively clear day (figs. 4.7 and 4.8).

On June 24th, the cloud cover averaged about three-tenths. As a result, direct radiation was dominant in all but 2200 and 2400 h. Throughout the day, negative net long-wave radiation prevailed, but there was also a diurnal cycle similar to those observed at the study site during most other clear days of the melt period. This energy loss was approximately  $-70 \text{ Wm}^{-2}$  in the early hours but decreased to  $-17 \text{ Wm}^{-2}$  at 1700 h. A reduced loss in long-wave radiation was due to increased incoming long-wave radiation since the radiation emitted from a melting snow surface was held constant. The net radiation balance was negative in the evening and early morning hours when the long-wave energy loss exceeded the net short-wave gain. Net radiation reached a maximum shortly after the solar radiation peak. A high net radiation value was sustained by a peak in the incoming long-wave radiation although the incoming solar radiation was in decline.

The radiation balance for slopes of four azimuths (north, south, east and west) with three gradients ( $10^\circ$ ,  $20^\circ$  and  $30^\circ$ ) are plotted in figure 4.8. For comparable slopes, the long-wave radiation balance is similar since the incoming long-wave radiation is a function only of slope angle. However, an increase in the slope angle from  $0^\circ$  to  $30^\circ$  only decreases the net long-wave balance by approximately  $3 \text{ Wm}^{-2}$ . Hence, short-wave radiation accounts for most of the variation in the net

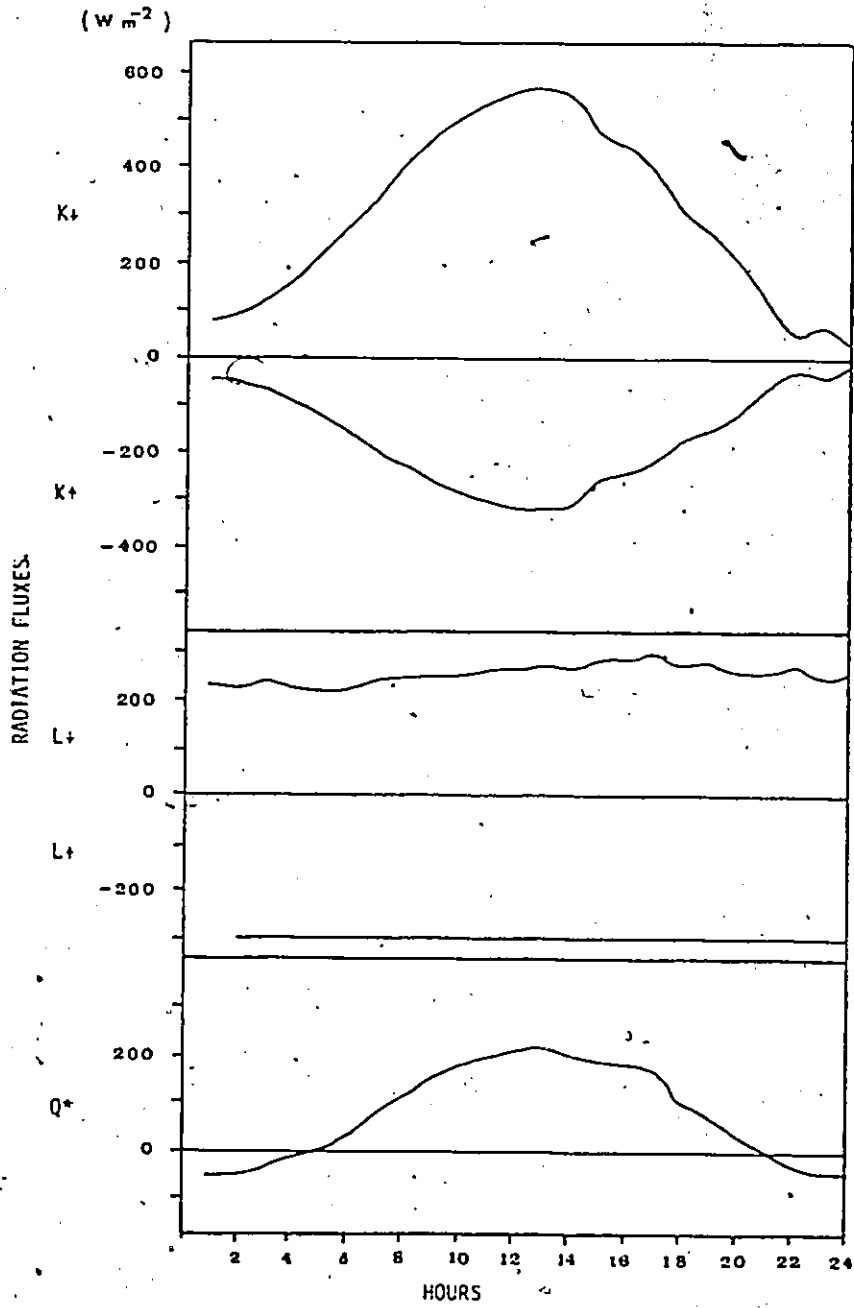


Fig. 4.7. Radiation balance on a horizontal surface on a clear day.

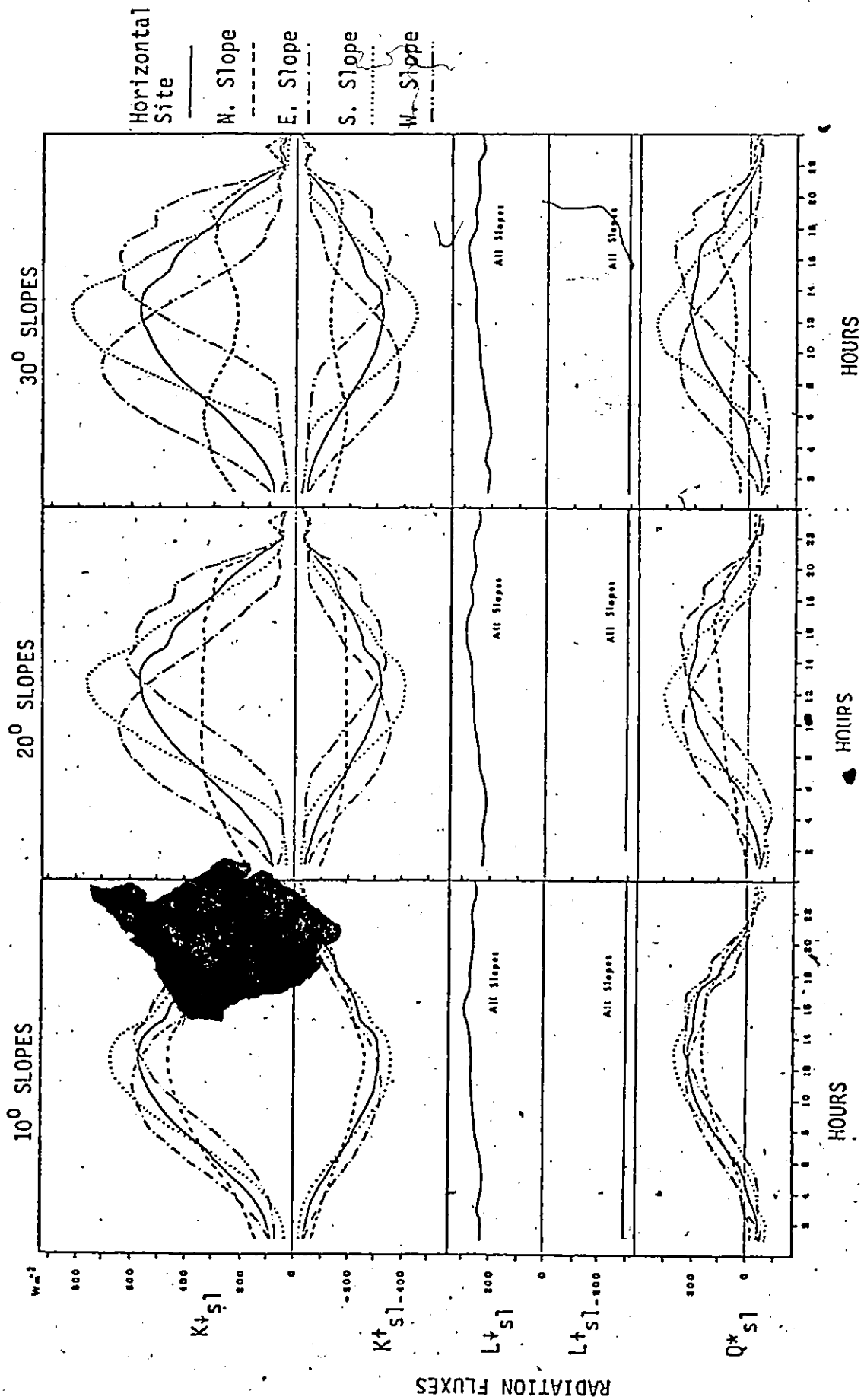


Fig. 4.8 Radiation Balance on Slopes of 10° to 30° on a clear day. Value for the horizontal site have been included for comparative purposes.

TABLE 4.1

TOTAL DAILY NET RADIATION AND SNOWMELT DUE TO  
RADIATION ON 12 SLOPES FOR A CLEAR DAY, JUNE 24, 1977

Daily Net Radiation ( $\text{MJ m}^{-2} \text{ day}^{-1}$ )

Slope Angle	Slope Azimuth			
	$0^{\circ}$	$90^{\circ}$	$180^{\circ}$	$270^{\circ}$
$0^{\circ}$	6.9			
$10^{\circ}$	6.3	7.1	7.2	6.4
$20^{\circ}$	5.5	7.1	7.7	5.8
$30^{\circ}$	4.6	7.2	8.2	5.6

Snowmelt Due to Radiation ( $\text{mm day}^{-1}$ )

Slope Angle	Slope Azimuth			
	$0^{\circ}$	$90^{\circ}$	$180^{\circ}$	$270^{\circ}$
$0^{\circ}$	20.5			
$10^{\circ}$	18.7	21.3	21.6	19.2
$20^{\circ}$	16.4	21.2	23.1	17.4
$30^{\circ}$	13.7	21.6	24.6	16.8

radiation balance.

As slope angle increases, the peak value of the incoming and reflected short-wave radiation increases for the south, east and west slopes. The east and west peaks also diverge from solar noon by about 1 hour for each  $10^{\circ}$  of slope angle. For the north slope, however, the incoming short-wave radiation decreases at noon but increases in the evening and early morning hours. At a  $30^{\circ}$  angle, there were two peaks in the incoming short-wave radiation for the north. For this slope, low values at noon are due to a smaller solar elevation of  $8^{\circ}$ .

The general pattern for the net radiation balance was similar to that of the incoming short-wave radiation, but with modification added by the net long-wave flux. Besides affecting the total daily net radiation, the long-wave flux seriously affects the net radiation balance when the slope is in shadow.

For south and west slopes with a  $30^{\circ}$  angle, shade is present during the early morning hours. This period corresponds with a maximum loss in long-wave radiation. For the  $30^{\circ}$  east slope, shadow occurs only in the evening when the long-wave loss is smaller.

As slope angle increases, the four azimuths receive most of their energy during different times of the day. Thus, large differences occur between slopes depending on cloud conditions and the long-wave radiation balance, as is illustrated by table 4.1. The daily totals of net radiation indicate that for this day (June 24, 1977), the energy income increased with slope angle for the east and south slopes while the opposite held for the west and north slopes. The reason was an increase



in cloud cover during the afternoon, thus reducing the amount of direct short-wave radiation. The west and north slopes with angles of  $20^\circ$  and  $30^\circ$  usually receive much of their energy from direct short-wave radiation in the afternoon, but since its magnitude was reduced by cloud cover, the prime source of energy input was diffuse radiation. For the entire day, therefore, the west slope received less direct solar radiation than the east slope though both received the same amount of diffuse radiation. In view of the late afternoon clouds, the north slope was affected in a manner similar to the west slope. The effect of clouds is more frequently encountered by northern slopes because around 2400 h, the sun is low in the sky and is affected by distant clouds and the atmosphere.

#### 4.3.3 Slope Radiation Balance on an Overcast Day

On an overcast day the net radiation on different slopes is minimized. Table 4.2 indicates the cumulative net radiation for 12 slopes on the overcast day of June 14, 1977. The differences between the slopes are small and are due almost entirely to the small amounts of direct solar radiation that was received at mid-day (fig. 4.9). The radiative fluxes to the slopes were similar because the radiation reflected from the adjacent horizontal surfaces compensated for the decreases in the receipts of diffuse radiation caused by the increasing slope angle. Since the snow albedo was the same for each slope, the radiative losses were also the same and the resulting net radiation displayed little difference with respect to slope.

#### 4.3.4 Computation of Snowmelt on Slopes

As given by equation 4.1, the melt energy on a slope ( $Q_{MS1}$ )

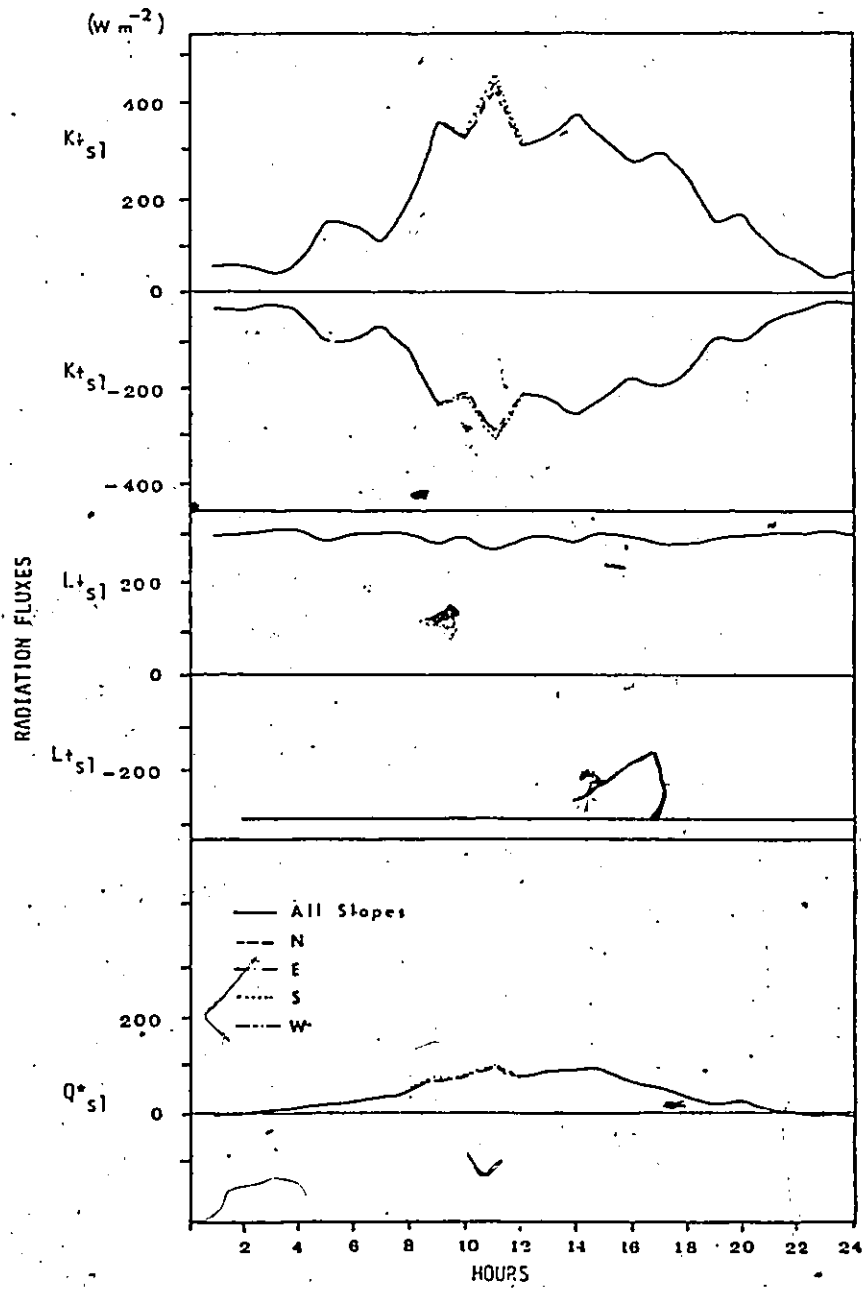


Fig. 4.9 Radiation balance on slopes during a cloudy day.

TABLE 4.2

TOTAL DAILY NET RADIATION AND SNOWMELT DUE TO  
RADIATION ON 12 SLOPES FOR AN OVERCAST DAY, JUNE 14, 1977

Daily Net Radiation ( $\text{MJ m}^{-2} \text{ day}^{-1}$ )

Slope Angle	Slope Azimuth			
	$0^{\circ}$	$90^{\circ}$	$180^{\circ}$	$270^{\circ}$
$0^{\circ}$	3.3			
$10^{\circ}$	3.3	3.3	3.4	3.3
$20^{\circ}$	3.3	3.4	3.4	3.3
$30^{\circ}$	3.2	3.4	4.3	3.3

Snowmelt Due to Radiation ( $\text{mm day}^{-1}$ )

Slope Angle	Slope Azimuth			
	$0^{\circ}$	$90^{\circ}$	$180^{\circ}$	$270^{\circ}$
$0^{\circ}$	9.9			
$10^{\circ}$	9.8	10.0	10.0	9.9
$20^{\circ}$	9.7	10.0	10.1	9.9
$30^{\circ}$	9.7	10.0	10.2	9.9

was partitioned into net radiation ( $Q_{s1}^*$ ), sensible heat flux ( $Q_H$ ), latent heat flux ( $Q_E$ ) and the energy added by precipitation ( $Q_p$ ). Only the  $Q_{s1}^*$  component is assumed to vary significantly with different slopes. Using the algorithm described earlier in this chapter,  $Q_{s1}^*$  was computed for some typical slopes in the vicinity of the study area. In this area, slope angles seldom exceed  $10^\circ$  except on the walls of incised valleys. Using a slope angle of  $10^\circ$ ,  $Q_{s1}^*$  was calculated for four azimuths of  $0^\circ$ ,  $90^\circ$ ,  $180^\circ$  and  $270^\circ$  and the cumulative values for the entire snowmelt period are plotted in figure 4.10. For the 15-day period being studied,  $Q_{s1}^*$  did not differ significantly between the four slopes (table 4.3), the largest difference being only 6 mm of melt or about 3 percent of the total contribution of  $Q_{s1}^*$ . Several factors contributed to the similarity of the total melt energy received by different slopes. For approximately half of the study period, diffuse radiation was the source of short-wave contribution and under these conditions, little difference is expected between the slopes. For the rest of the study period, some cloud was always present and since the sun never sets, the timing of the cloud cover was critical. On June 21st, for example, the sky was overcast most of the day, but cleared up in the evening. This resulted in the north slope receiving the most radiant energy while the south slope received the least. It appears that, over the course of the study period, the movement of the cloud cover tended to minimize the differences between the slopes.

Since the other components of the slope energy balance were assumed not to vary, then the difference in the calculated slope snow-

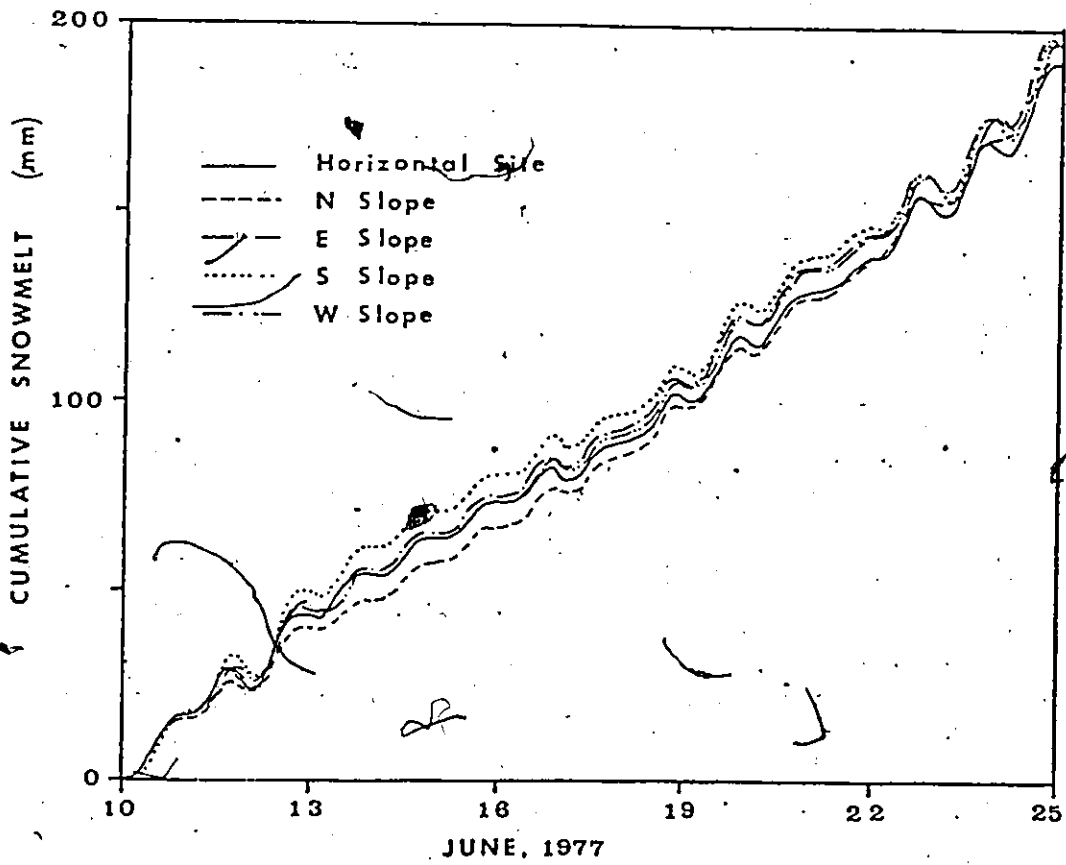


Fig. 4.10 Cumulative snowmelt due to radiation on  $10^\circ$  slopes during the study period.

TABLE 4.3  
DAILY NET RADIATION AND CUMULATIVE SNOWMELT DUE NET RADIATION

June	Horz.*	Daily Net Radiation MJ m <sup>2</sup> day <sup>-1</sup>					Horz.	Cumulative Melt mm (W.E.)				
		10° Slopes						10° Slopes				
		N	E	S	W	W		N	E	S	W	
10	5.6	5.2	5.6	5.9	5.4	16.8	15.6	16.7	17.5	16.3		
11	3.2	2.6	2.5	3.6	3.7	26.3	23.4	24.4	28.3	27.2		
12	6.4	5.6	6.3	7.0	6.3	45.5	40.2	43.2	49.4	46.2		
13	3.3	2.4	3.7	3.9	2.7	55.3	47.6	54.2	61.2	54.3		
14	3.3	3.3	3.3	3.3	3.3	65.3	57.3	64.0	70.9	64.1		
15	3.2	3.2	3.1	3.1	3.2	74.8	66.8	73.2	80.3	73.6		
16	3.1	3.4	2.6	2.8	3.5	84.2	77.0	81.1	88.6	84.2		
17	2.9	3.0	3.0	2.7	2.7	92.8	85.9	90.0	96.8	92.2		
18	4.1	4.3	3.8	3.8	4.3	105.1	98.8	103.1	108.1	105.1		
19	5.5	5.1	5.2	5.8	5.7	121.7	114.0	116.9	125.3	122.2		
20	4.7	4.8	4.5	4.4	4.7	135.7	128.3	130.4	138.4	136.3		
21	3.2	3.4	3.0	2.9	3.3	145.3	138.6	139.5	146.9	146.2		
22	4.5	5.1	4.2	3.7	4.6	158.7	153.9	152.2	158.1	159.9		
23	5.6	5.8	5.6	5.3	5.4	175.4	171.2	168.8	173.9	176.2		
24	6.9	6.3	7.1	7.2	6.4	195.9	189.9	190.1	195.5	195.4		

\* Horizontal

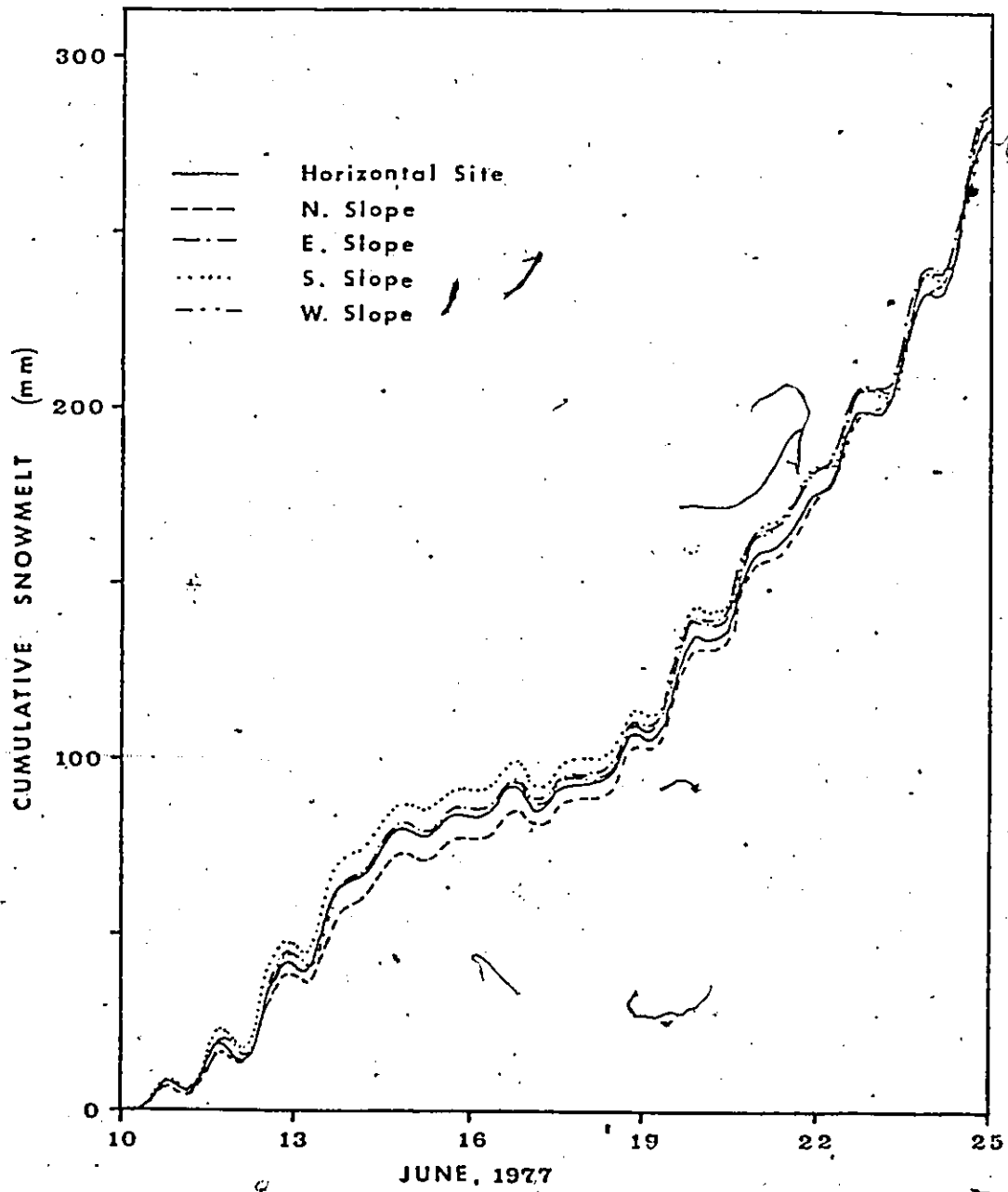


Fig. 4.11 Cumulative snowmelt on 10° slopes during the study period.

melt energy ( $Q_{MS1}$ ) between slopes remained the same but its relative magnitude decreased to approximately 2 percent (fig. 4.11). Although snow ablation measurements were made on the four slopes, the results were not sufficiently accurate to confirm these results.

The above computations have been performed with the assumption that the fluxes of sensible and latent heat are identical for all slopes. However, the results of section 3.5 indicate that the local advection of heat energy occurs when bare ground is present. Thus some spatial variation in these fluxes is to be expected, with their magnitude being related to the location of the bare ground, the wind direction and fetch. Topography will also cause local variations in the wind speed, thus affecting the transfer of sensible and latent heat. However, when these are important components in the energy balance, they should be calculated in slope energy balance computations.

Goodison (1972) noted that a relationship between the incident short-wave radiation flux and snow ablation could not be demonstrated for his site. He indicated that, while a more complete radiation balance should be calculated, an estimate of the fluxes of sensible and latent heat should also be included in the slope energy balance. The results of Price et al (1976) show that this is a reasonable approach. However, to improve the estimation of snowmelt on slopes, the spatial variability of the fluxes of sensible and latent heat should be examined in more detail.



## CHAPTER FIVE

### CONCLUSION

Previous energy balance studies during the snowmelt period at Arctic tundra sites suggested that the net radiation provides most of the energy consumed in melting snow. This study shows that the flux of sensible heat is also a major source of heat because in 1977, it supplied over 40 percent of the energy used in snowmelt and evaporation while net radiation supplied the remainder. Of the energy provided, 20 percent was used for evaporation and the rest produced snowmelt.

Diurnal cycles were commonly observed in the fluxes of energy, but the amplitude of these cycles was reduced during cloudy days. The magnitude of the various fluxes also varied greatly from day to day. For the entire study period, however, there was a tendency for the latent heat flux to decrease and the sensible heat flux to increase, but no trend was apparent for net radiation. At the end of the snowmelt period, the advection of energy from bare ground towards the snowcover is found to be more important than previously realized. As warm air above the bare ground moved over the snowcover, large horizontal and vertical temperature gradients were induced.

For the horizontal site, the computed snowmelt values compare favourably with the observed ablation rate, showing that the energy balance approach can reliably estimate the snowmelt at a High Arctic site. However, it is necessary to ensure that when the snowcover is patchy, both the temperature and humidity sensors are located within the boundary layer.

An extension of snowmelt computations to various slopes indicated that for slope angles of up to  $10^{\circ}$  the rate of snowmelt was similar regardless of aspect. On a clear day, maximum difference in the flux of incoming radiation was 13 percent and it occurred between north and south slopes. On overcast days the difference was minimized. Since snow ablation measurements for the slope sites are inadequate, the accuracy cannot be verified. On a daily basis, the computation procedure described enables a determination of the timing of snowmelt on various slopes. Over a period of days, the total snowmelt computed for a horizontal site will adequately estimate the melt rate on low angle slopes.

## REFERENCES

- Allen, L.E., 1974. A Sub-alpine Snowmelt Runoff Model. Ph.D. Thesis, University of Wyoming, 407.
- Anderson, E.A., 1967. A Point Energy and Mass Balance of a Snow Cover, U.S. Dept. of Commerce, NOAA Technical Report NWS 19, 151.
- Arnfield, A.J., 1975. A note on the diurnal, latitudinal and seasonal variation of the surface reflection coefficient. J. App. Met., 14, 1603-1608.
- Aufdenberge, T.P., 1974. Energy balance studies over glacier and tundra surfaces, Chitistone Pass, Alaska, summer 1969, American Geographical Society, Icefield Ranges Research Project Scientific Results, Vol. 4, 63-79.
- Cogley, J.G., 1975. Properties of Surface Runoff in the High Arctic. Ph.D. Thesis, McMaster University, 358.
- Cox, L.M. and Zuzel, J.F., 1976. A method for determining sensible heat transfer to late lying snowdrifts. Proc. Western Snow Conf., 44, 23-28.
- Dept. of Transport, 1967. The Climate of the Canadian Arctic. Meteorological Branch, Air Services, Dept. of Transport (Canada), 32.
- Dept. of Transport, 1974. The Climate of the Canadian Arctic. Meteorological Branch, Air Services, Dept. of Transport (Canada).
- DeWalle, D.R. and Meiman, J.R., 1971. Energy exchange and late season snowmelt in a small opening in a Colorado sub-alpine forest. Water Resources Res., 7, 184-188.
- Föhn, P.M.B., 1973. Short-term snowmelt and ablation derived from heat and mass balance measurements. J. Glaciol., 12, 275-290.
- Garnier, B.J. and Ohmura, A., 1968. A method of calculating the direct short-wave radiation income on slopes. J. App. Met., 7, 796-800.
- Garnier, B.J. and Ohmura, A., 1970. The evaluation of surface variation in solar radiation income. Solar Energy, 13, 21-34.
- Giddings, J.G. and La Chapelle, E., 1963. Diffusion theory applied to radiant energy distribution and albedo of snow. J. Geophys. Res., 66, 181-189.

- Gold, L.W. and Williams, G.P., 1961. Energy balance during the snowmelt period at an Ottawa site. International Association for Scientific Hydrology, 54, 288-294.
- Goodison, B., 1972. The Distribution of Global Radiation over Peyto Glacier, Alberta. Scientific Series, 22, Inland Waters Directorate, Environment Canada, 22.
- Granger, R.J. and Male, D.H., 1977. Melting of a Prairie Snowpack, in Second Conference on Hydrometeorology, Toronto, American Meteorological Society and Canadian Meteorological and Oceanographic Society, 261-267.
- Granger, R.J., 1977. Energy Exchange During Melt of a Prairie Snowcover. M.Sc. Thesis, University of Saskatchewan (Saskatoon), 122.
- Hubley, R.C., 1955. Measurements of diurnal variation in snow albedo on Lemon Creek Glacier, Alaska. J. Glaciol., 2, 560-563.
- Kondratyev, K. Ya., 1969. Radiation in the Atmosphere. Academic Press, New York, 912.
- La Casinière, A.C. de, 1974. Heat exchange over a melting snow surface. J. Glaciol., 13, 55-72.
- La Chapelle, E., 1959. Annual mass and energy exchange on the Blue Glacier. J. Geophys. Res., 64, 443-449.
- Leaf, C.F., 1966. Free water content of snowpack in sub-alpine areas. Proc. Western Snow Conf., 34, 17-24.
- Lister, H., 1962. Heat and mass balance at the surface of the Ward Hunt Ice Shelf, Ellesmere Island. Research Paper 19, Arctic Institute of North America.
- Lougeay, R., 1974. Microclimatological studies over the Seward Glacier snowpack. Icefield Ranges Research Project Scientific Results, 2, 17-26.
- Lourence, F.J. and Priddy, W.O., 1969. A psychrometer for micro-meteorological profile determination. J. App. Met., 8, 492-498.
- Marsh, P., 1978. Water Balance of a Small High Arctic Basin. M.Sc. Thesis, McMaster University, 108.
- McCann, S.B. and Cogley, J.G., 1972. Hydrological observations on a small Arctic catchment, Devon Is. Can. J. Earth Sci., 9, 361-365.
- McKay, D.C. and Thurtell, G.W., 1978. Measurements of the energy fluxes involved in the energy budget of a snow cover. J. App. Met., 17, 339-349.

- Müller, F. and Keeler, C.M., 1969. Errors in short-term ablation measurements on melting ice surfaces. J. Glaciol. 8, 91-105.
- Obled, Ch. and Rosse, B., 1977. Mathematical models of a melting snowpack at an index plot. J. Hydrology, 32, 139-163.
- Ohmura, A., 1972. Some climatological notes on the expedition area. Axel Heiberg Island Research Reports, Miscellaneous Papers, McGill University, Montreal, 5-13.
- Ohmura, A., and Muller, F., 1976. Heat measurements on Arctic tundra, in International Geography, Climatology, Hydrology and Glaciology, Section 2, XXIII International Geographical Conference, Moscow, 80 - 84.
- O'Neill, A.D.J., 1973. The Energetics of Shallow Prairie Snowpacks. Ph.D. Thesis, University of Saskatchewan (Saskatoon), 197.
- Orvig, J., 1954. Glacial-meteorological observations on ice caps in Baffin Island. Geog. Ann., 36, 193-318.
- Petzold, D.E., 1977. An estimation technique for snow surface albedo. Climatological Bulletin, McGill Univ., 21, 1-11.
- Price, A.J. Dunne, T. and Colbeck, S.C., 1976. Energy balance and runoff from a subarctic snowpack. U.S. Army Corps. of Eng., CRREL Report 76-26.
- Price, A.J. and Dunne, T., 1976. Energy balance computations in a subarctic area. Water Resources Res., 12, 686-
- Price, A.J., 1977. Snowmelt runoff processes in a subarctic area. McGill Sub-arctic Res. Paper, 29, McGill University, 106.
- Ryden, B.E., 1977. Hydrology of Truelove Lowland. in Truelove Lowland Devon Is., Canada: A High Arctic Ecosystem, ed. L.G. Bliss, University of Alberta Press, 107-136.
- Streten, W.A. and Wendler, G., 1968. The mid-summer heat balance of an Alaskan Maritime glacier. J. Glaciol., 7, 431-440.
- Swift, L.W., 1976. Algorithm for solar radiation on mountain slopes. Water Resources Res., 12, 108-112.
- U.S. Army, 1956. Snow Hydrology: Summary Report of the Snow Investigation. North Pacific Division, Corps of Eng., 437.
- Weisman, R.N., 1977. Snowmelt: A two dimensional turbulent Diffusion Model. Water Resources Res., 13, 337-342.
- Weller, G. Cubley, S., Parker, S., Trabant, D., Benson, C., 1972. The tundra microclimate during snowmelt at Barrow, Alaska. Arctic, 25,

- Weller, G. and Holmgren, B., 1974. The microclimates of the Arctic Tundra. J. App. Met., 13, 854-862.
- Wendler, G., 1967. The heat balance at the snow surface during the melting period (March-April 1966) near Fairbanks, Alaska. Gerlands Beitr. Geophys., 76, 453-460.
- Wendler, G., and Ishikawa, N., 1973. Experimental study of the amount of ice melt using three different methods: A contribution to the International Hydrological Decade. J. Glaciol., 12, 399-410.
- Williams, L.D., Barry, R.G. and Andrews, J.T., 1972. Application of computed global radiation for areas of high relief. J. App. Met., 11, 526-533.
- Woo, M.K., 1976. Hydrology of a small Canadian High Arctic basin during the snowmelt period. Catena, 3, 155-168.
- Yosida, Z., 1960. A calorimeter for measuring the free water content of wet snow. J. Glaciol., 3, 574-576.

## APPENDIX 1

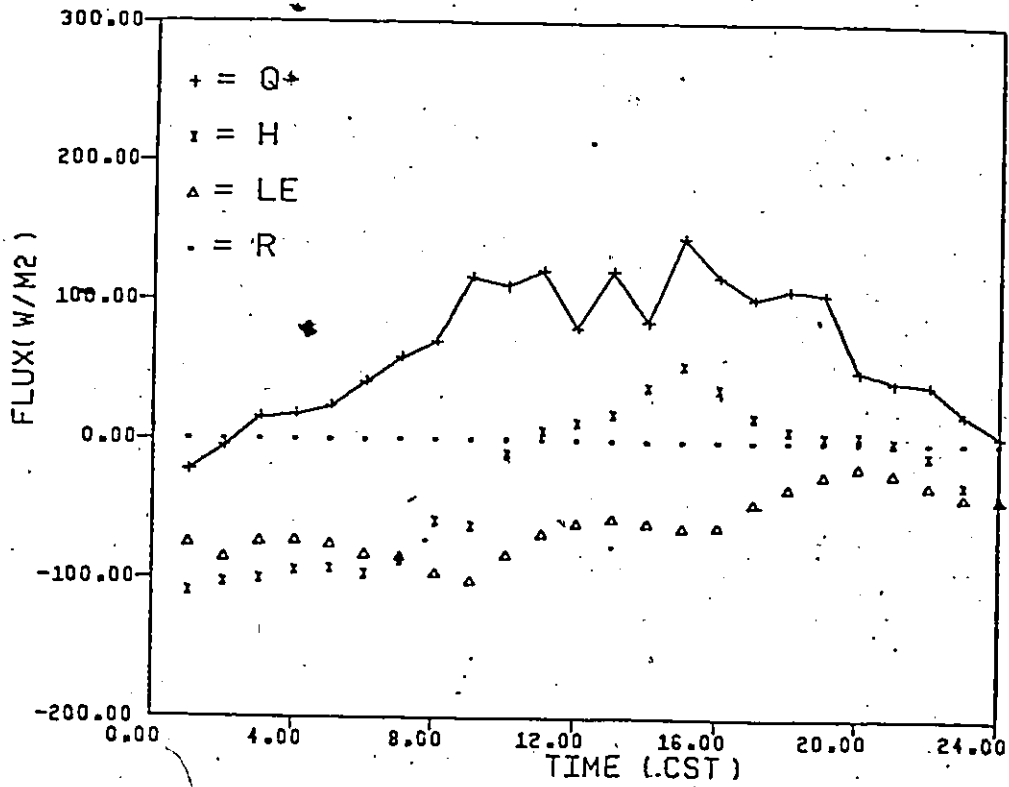
## HOURLY COMPONENTS OF THE SNOW SURFACE ENERGY BALANCE

JUNE 10, 1977 to JUNE 24, 1977

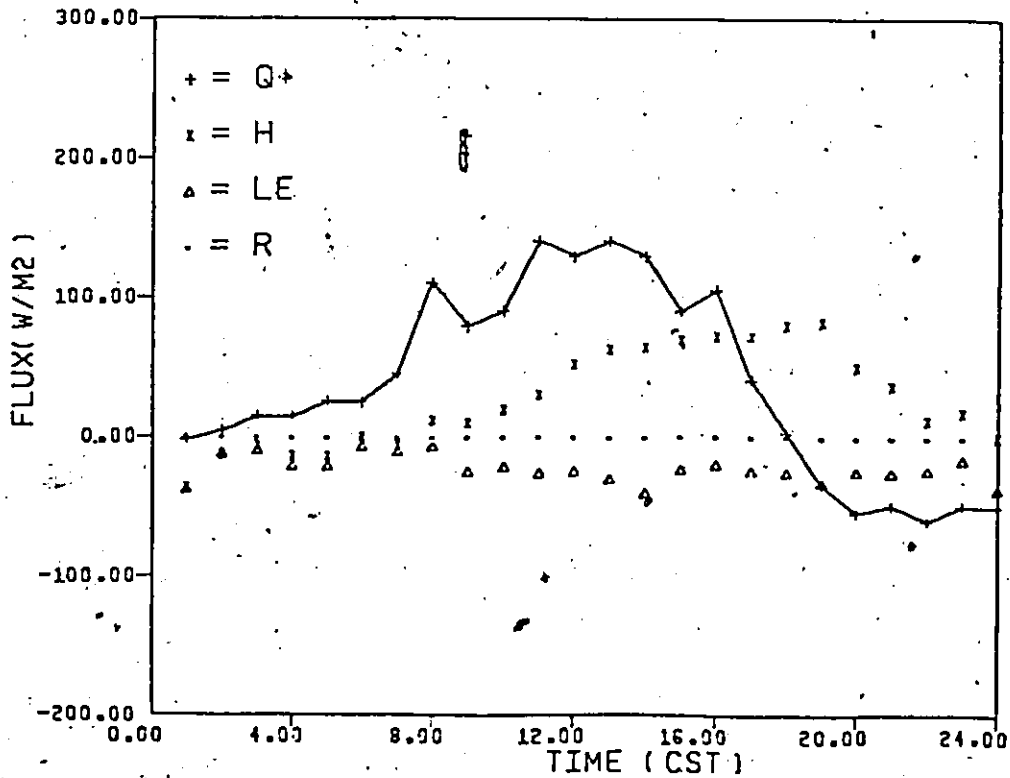
In the following diagrams,  $Q^*$  is the net radiation flux,  $H$  the sensible heat flux,  $LE$ , the latent heat flux, and  $R$  the energy added by precipitation.

78

RESOLUTE, 10 JUN 1977

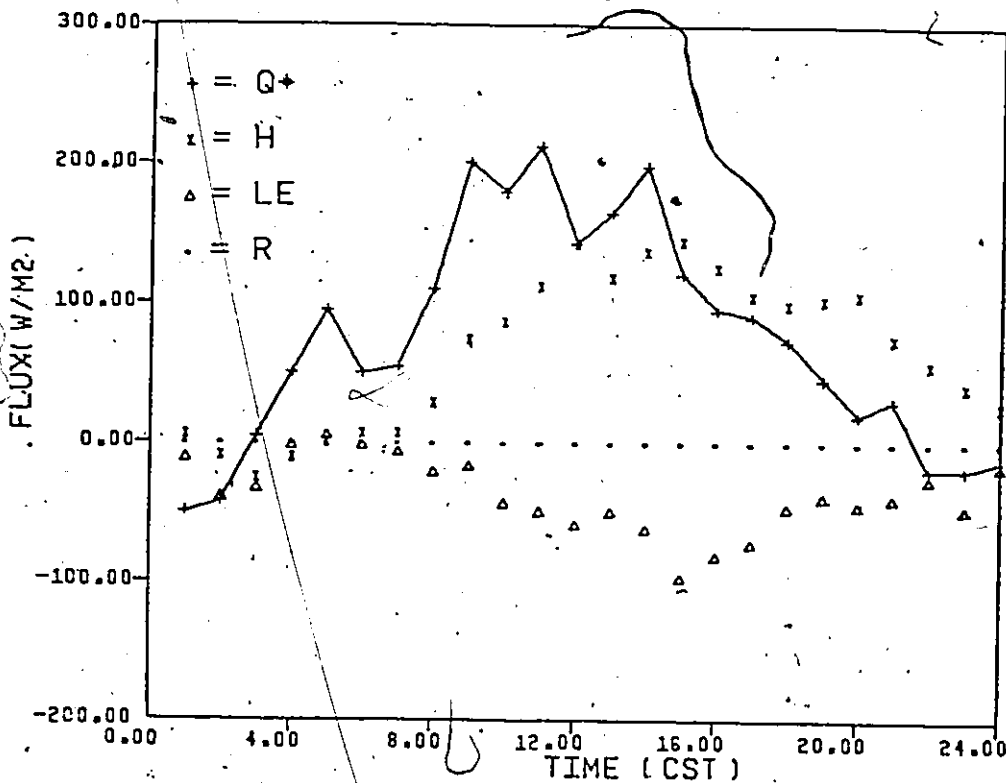


RESOLUTE, 11 JUN 1977

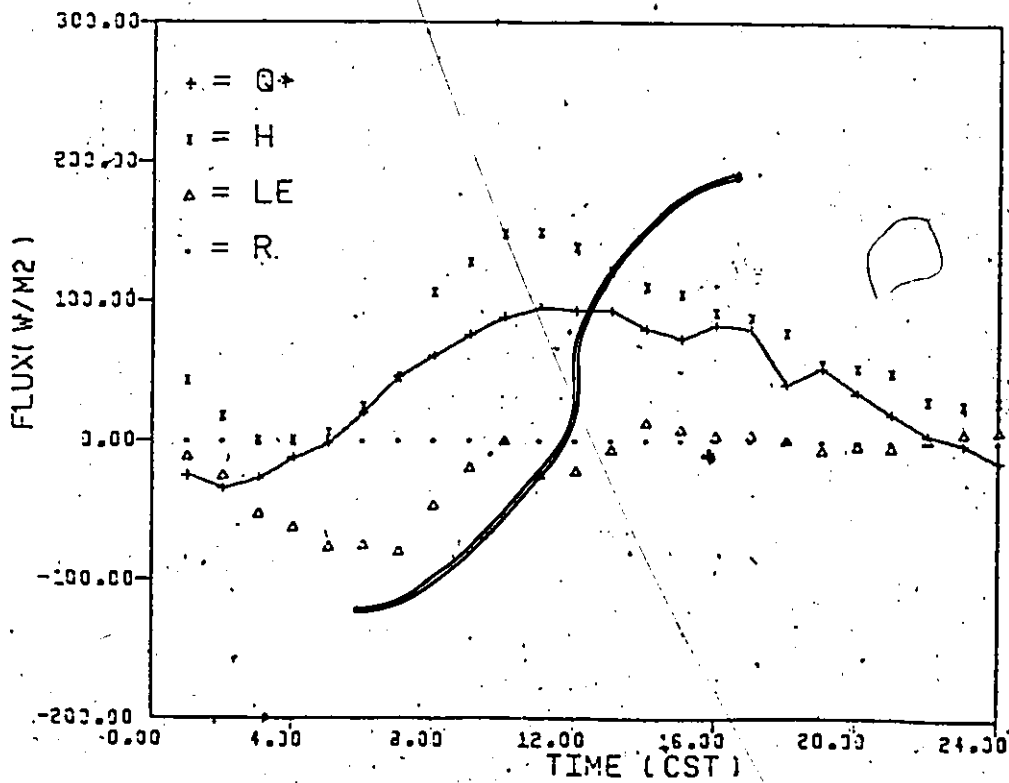




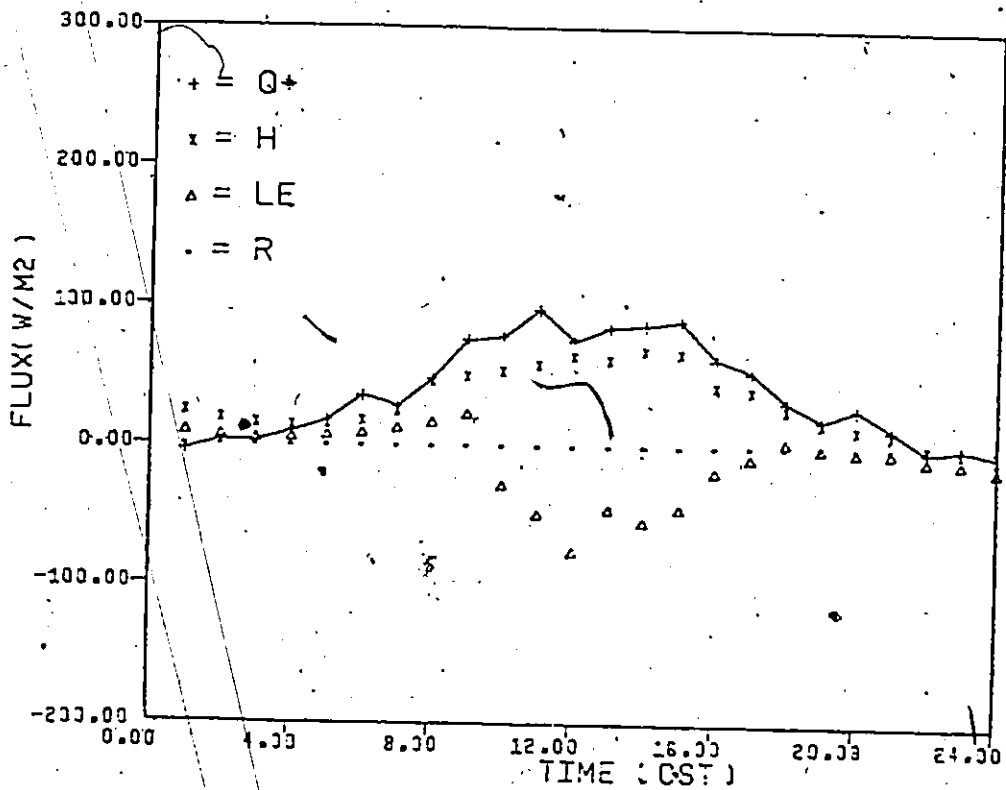
RESOLUTE, 12 JUN 1977



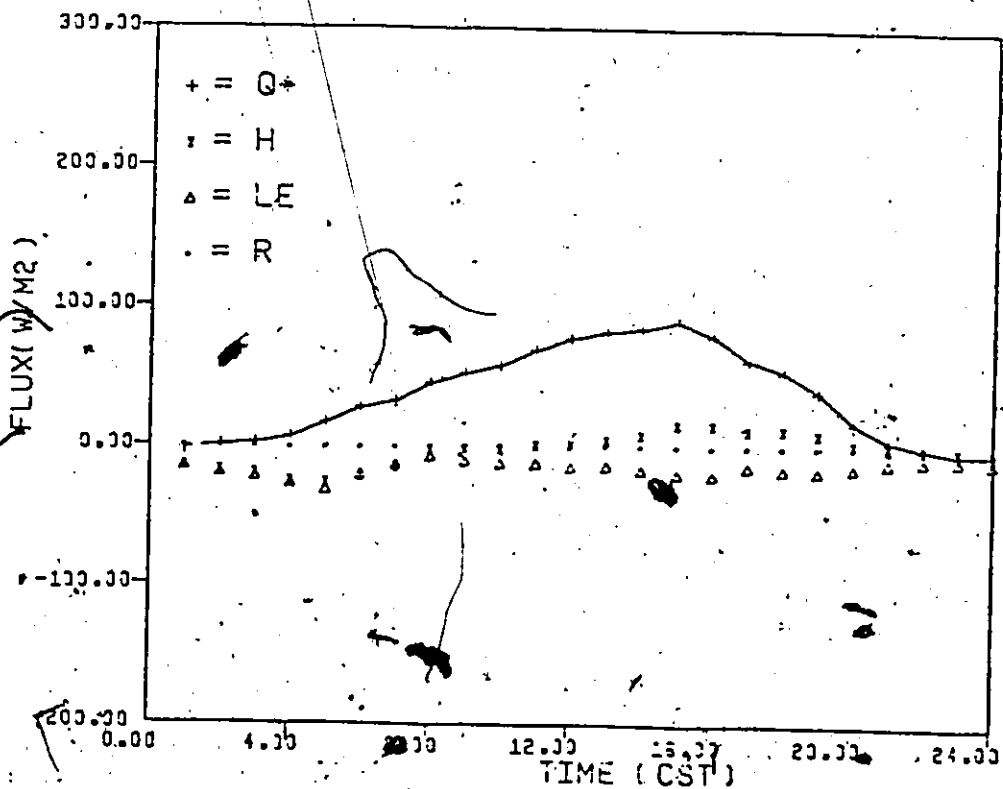
RESOLUTE, 13 JUN 1977



RESOLUTE, 14 JUN 1977

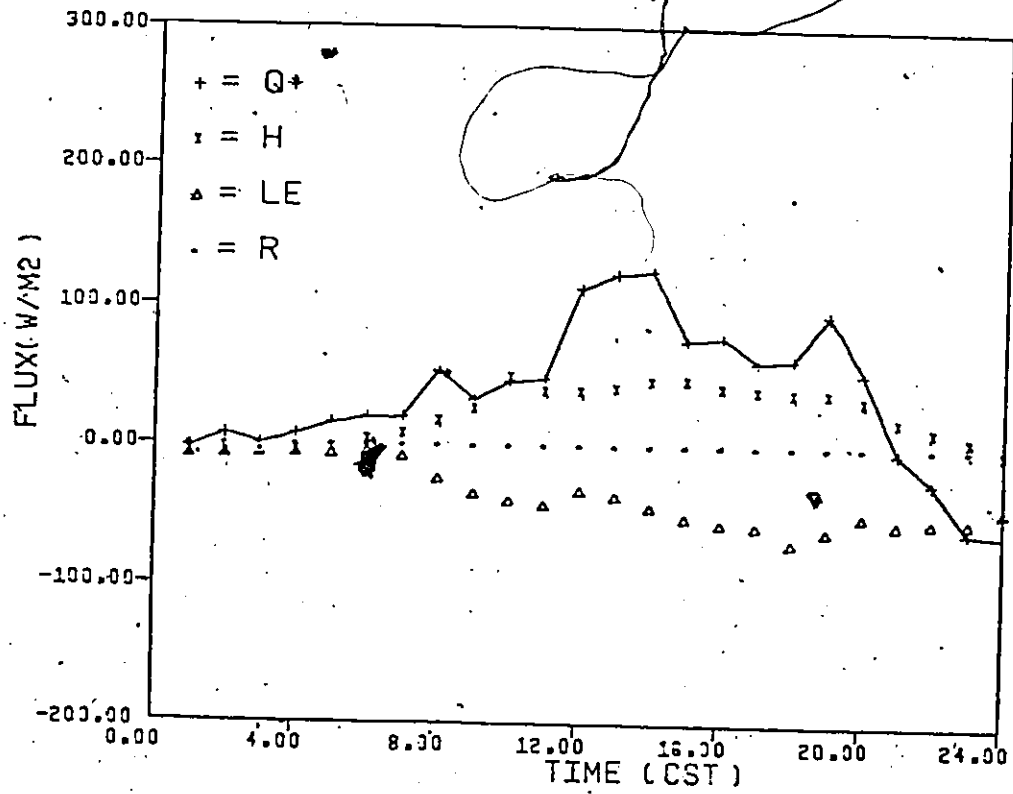


RESOLUTE, 15 JUN 1977

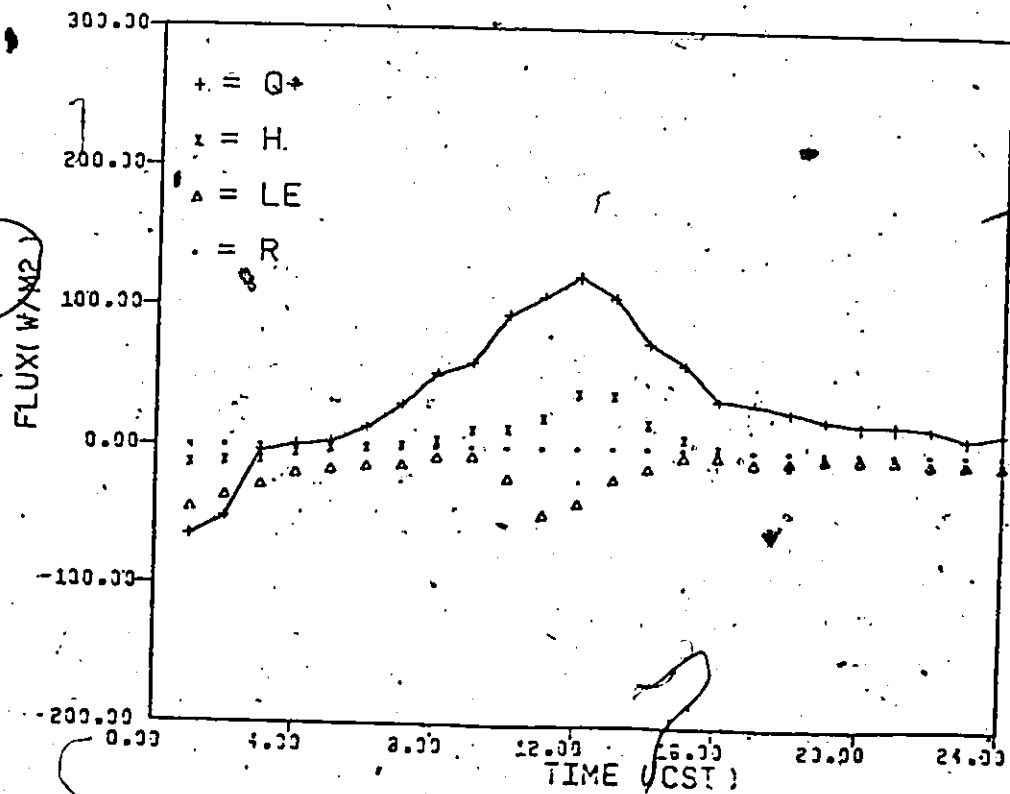


81

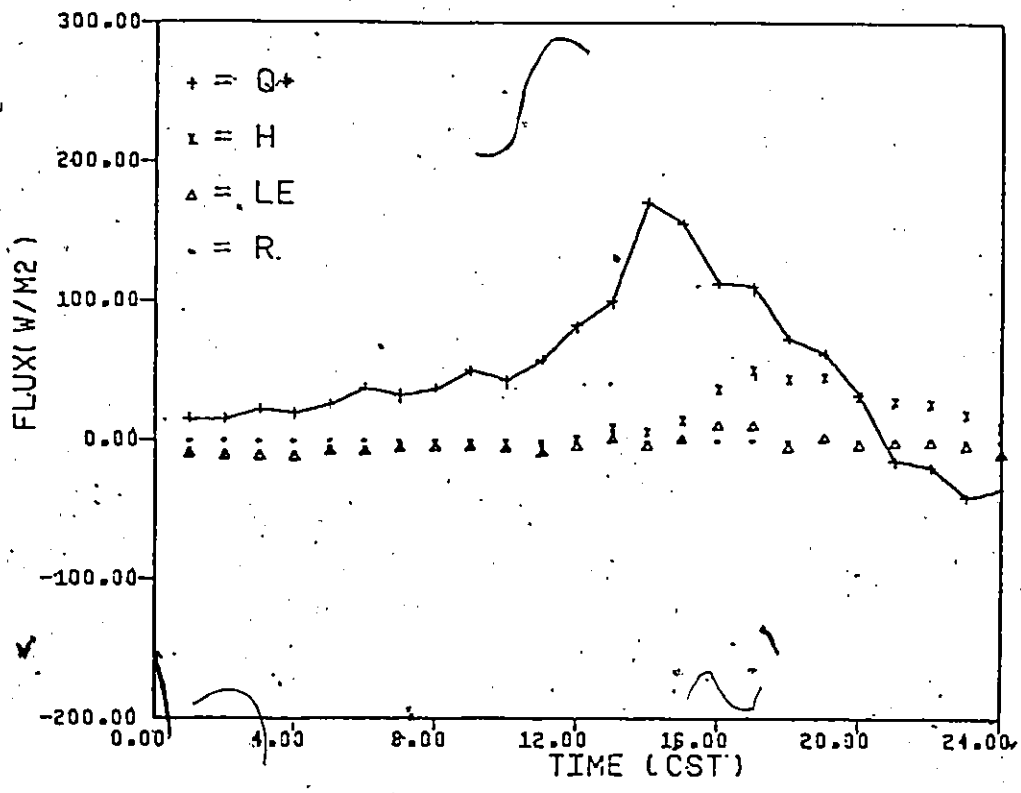
RESOLUTE, 16 JUN 1977



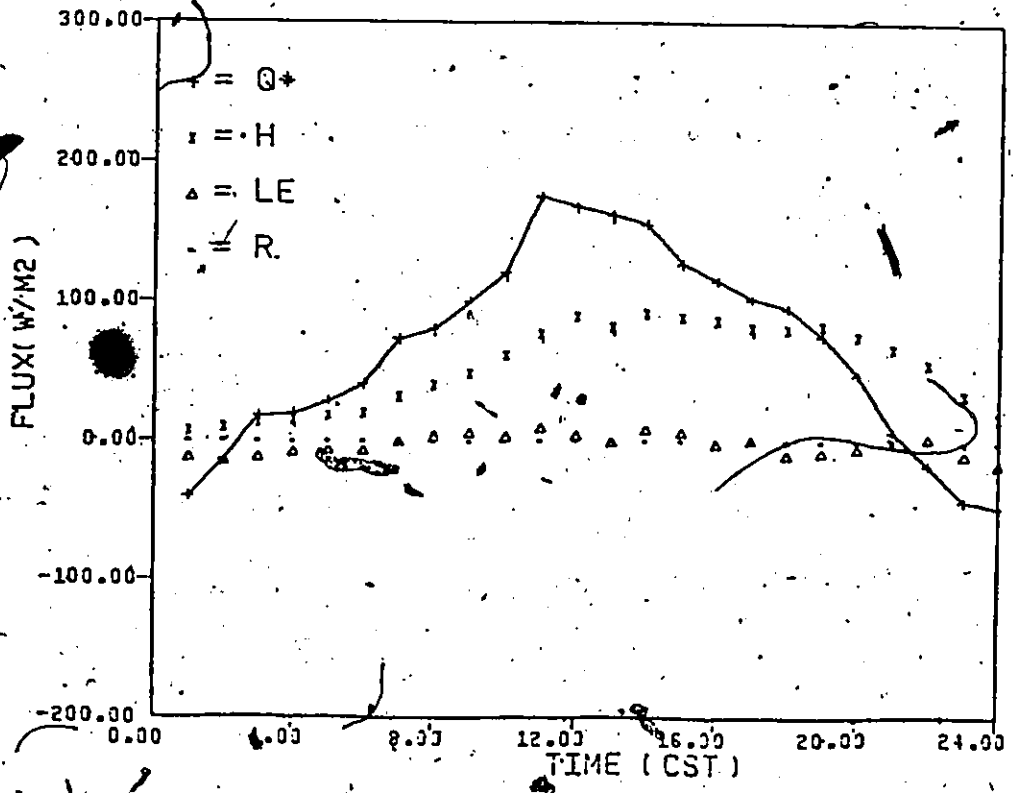
RESOLUTE, 17 JUN 1977



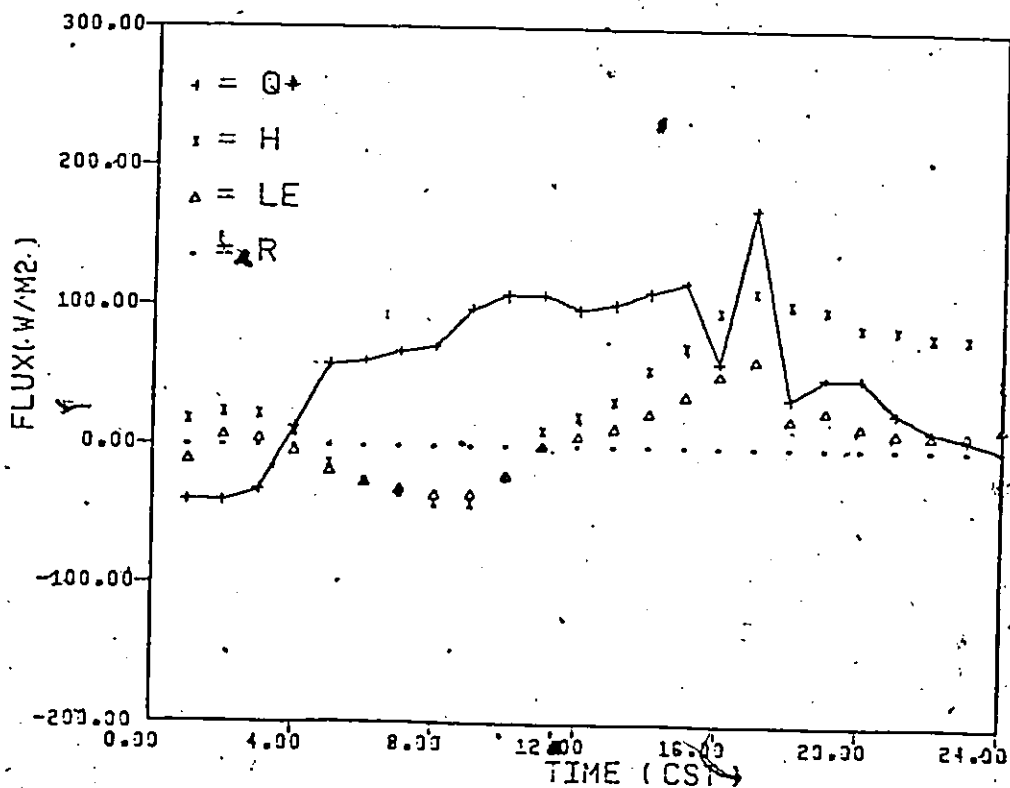
RESOLUTE, 18 JUN 1977



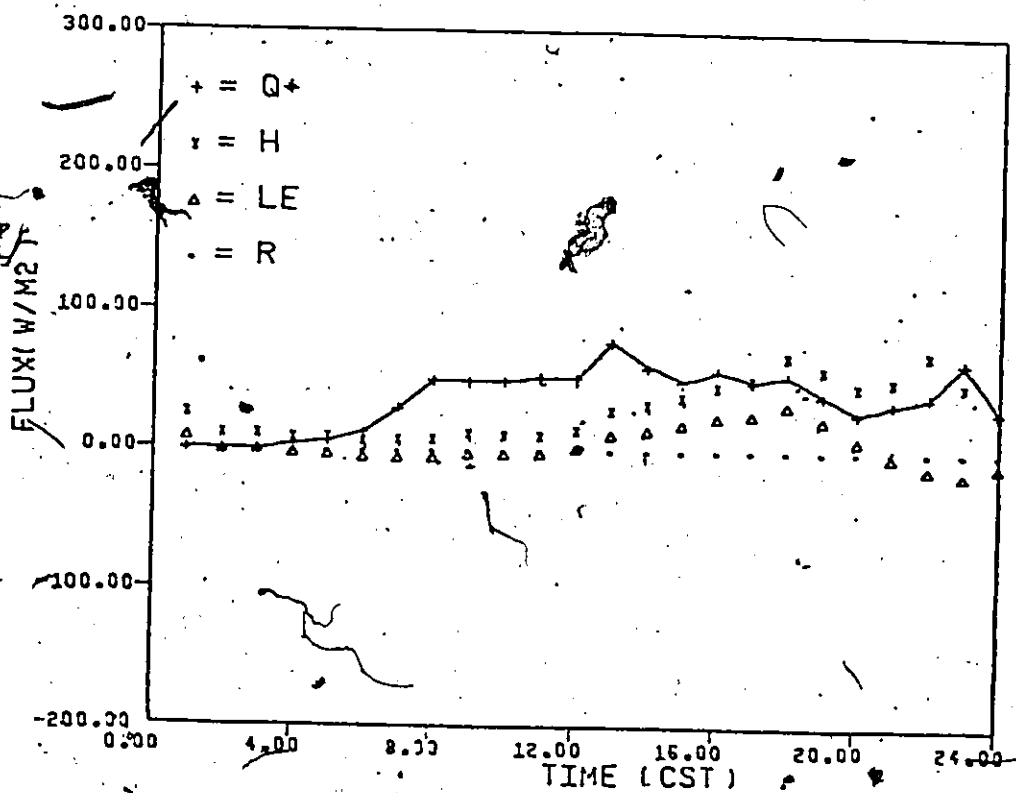
RESOLUTE, 19 JUN 1977



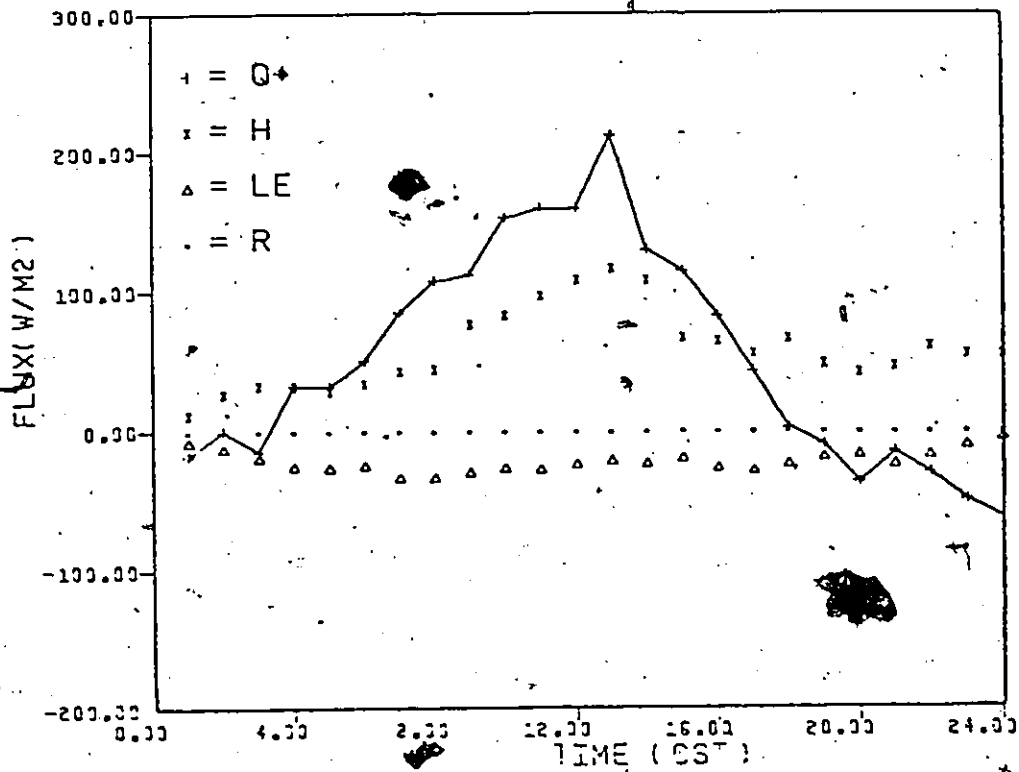
RESOLUTE, 20 JUN 1977



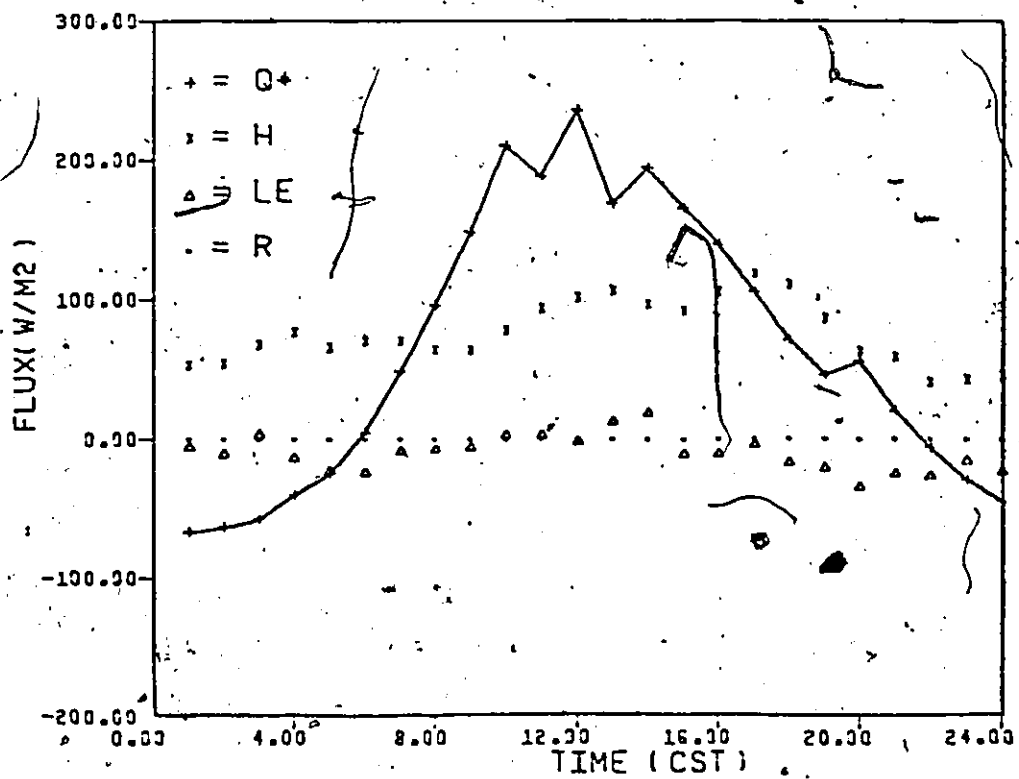
RESOLUTE, 21 JUN 1977



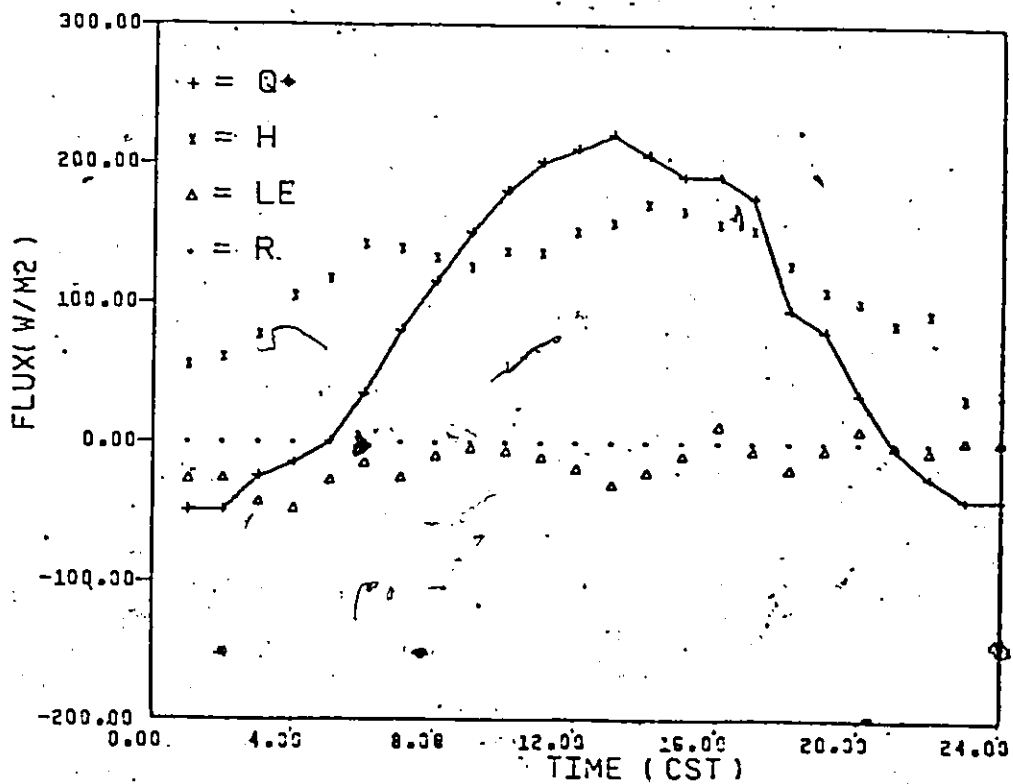
RESOLUTE, 22 JUN 1977



RESOLUTE, 23 JUN 1977



RESOLUTE, 24 JUN 1977



## APPENDIX TWO

## NOTATION

## Upper Case Roman

A	slope azimuth	degrees
$C_D$	drag coefficient	dimensionless
$C_H$	drag coefficient for sensible heat transfer	dimensionless
$C_E$	drag coefficient for latent heat transfer	dimensionless
D	diffuse solar radiation flux	$Wm^{-2}$
$D_{sl}$	diffuse solar radiation flux on a slope	$Wm^{-2}$
E	solar elevation	degrees
H	hour angle	degrees
$I_0$	solar constant	$Wm^{-2}$
$I_{sl}$	direct short-wave radiation flux on a slope	$Wm^{-2}$
$I_h$	direct short-wave radiation flux on a horizontal surface	$Wm^{-2}$
J	days since June 7th	day
$K^*$	net short-wave radiation flux	$Wm^{-2}$
$K_+$	incident short-wave radiation flux	$Wm^{-2}$
$K_r$	reflected short-wave radiation flux	$Wm^{-2}$
$L^*$	net long-wave radiation flux	$Wm^{-2}$
$L_+$	downward atmospheric long-wave radiation flux	$Wm^{-2}$
$L_e$	emitted long-wave radiation flux	$Wm^{-2}$
$L_{rh}$	long-wave radiation flux reflected from a horizontal surface	$Wm^{-2}$
$L_{eh}$	long-wave radiation flux emitted from a horizontal surface	$Wm^{-2}$
M	snow ablation	mm



P	atmospheric pressure	Pa
$Q^*$	net radiation flux	$Wm^{-2}$
$Q_M$	surface energy balance	$Wm^{-2}$
$Q_H$	sensible heat flux	$Wm^{-2}$
$Q_E$	latent heat flux	$Wm^{-2}$
$Q_p$	energy flux due to precipitation	$Wm^{-2}$
R	precipitation intensity	$m\ s^{-1}$
$R_e$	ratio of earth's radius to the atmospheric thickness	dimensionless
$R_i$	Richardson number	dimensionless
$R_{sl}$	flux of short-wave radiation reflected from a horizontal surface	$Wm^{-2}$
S	slope angle	degrees
T	snow thermal quality	dimensionless
U	A.E.S. wind speed at 10 m	$m\ s^{-1}$
Z	zenith angle	degrees

Lower Case Roman

a	empirical coefficients	degree <sup>-1</sup>
$b_1, b_2$	empirical coefficients	dimensionless
$c_p$	heat capacity of air at a constant pressure	$J\ m^{-3}\ K^{-1}$
$c_w$	specific heat of water	$J\ kg^{-1}\ K^{-1}$
$c_1$ to $c_3$	temporary variables	
d	Julian date	
e	vapour pressure	Pa
$f_1$	empirical coefficients	dimensionless
$f_2$	empirical coefficients	degree <sup>-1</sup>

g	acceleration due to gravity	$m s^{-2}$
h	snow surface lowering	mm
i	angle of incidence between sun's rays and a surface	degrees
k	von Karman constant	dimensionless
m	optical air mass	dimensionless
$m_c$	water equivalent mass of the calorimeter	g
$m_s$	mass of the snow	g
$m_w$	mass of the water	g
p	atmospheric transmissivity	dimensionless
r	radius vector of the Earth's orbit	dimensionless
u	wind speed	$m s^{-1}$
$u_m$	wind speed at the study site	$m s^{-1}$
z	height above the surface	m
$z_0$	surface roughness coefficient	m
Greek		
$\alpha$	albedo	dimensionless
$\alpha_0$	estimated daily minimum albedo at high solar elevations	dimensionless
$\epsilon$	ratio of molecular weight of water to air, constant equal to 0.622	dimensionless
$\gamma$	empirical coefficient	dimensionless
$\lambda$	latent heat of vapourization	$J kg^{-1}$
$\lambda_a$	apparent heat of fusion	$J kg^{-1}$
$\lambda_f$	heat of fusion	$J kg^{-1}$
$\zeta$	solar declination	radians
$\delta$	surface emissivity	dimensionless

$\phi$	latitude	degrees
$\rho_a$	density of air	$\text{kg m}^{-3}$
$\rho_s$	density of snow	$\text{kg m}^{-3}$
$\rho_w$	density of water	$\text{kg m}^{-3}$
$\sigma$	Steffan-Boltzman constant	$\text{m}^{-2} \text{K}^{-4}$
$\theta$	air temperature	K
$\theta_f$	final temperature	K
$\theta_i$	initial temperature	K
$\theta_R$	temperature of the precipitation	K

#### Subscripts

z	refers to measurement height z, above the surface
s	refers to surface measurements
sl	indicates quantities applicable to slopes
h	indicates quantities applicable to a horizontal surface